Low-Speed Space Launch System Computational Fluid Dynamics: A Comprehensive Overview

Brent Pomeroy,* Steven Krist,† Thomas Wignall,‡ Michael Lee,§ Karen Deere,†
and Farhad Ghaffari¶
NASA Langley Research Center, Hampton, Virginia 23681

In this review paper, low-speed computational work from NASA Langley Research Center in support of the Space Launch System (SLS) is discussed. This information includes both historical and present efforts with the Kestrel computational fluid dynamics solver. The low-speed aerodynamics of SLS is highly complex, and the analysis of the unsteady flowfield requires significant computational efforts. The SLS mission profile varies from the vehicle static on the launch pad through high-speed ascent. This study focuses on the prelaunch as well as liftoff and transition portions of the flight both in proximity to the launch tower and in isolation. High-alpha conditions, as large as 90 deg, result in a flowfield dominated by massive, large-scale flow separation and asymmetric vortices. High-fidelity solutions require an unsteady computational formulation to accurately capture the aerodynamics of the vehicle. A detailed discussion of the computational approach is presented, followed by key efforts to support the program, both historic and present, including information that has been either published previously or that has never before been published external to NASA.

Nomenclature

C_A	=	axial force coefficient (missile axis coordinate system)
C_l	=	rolling moment coefficient (missile axis coordinate system)
C_m	=	pitching moment coefficient (missile axis coordinate system)
C_N	=	normal force coefficient (missile axis coordinate system)
C_n	=	yawing moment coefficient (missile axis coordinate system)
C_Y	=	side force coefficient (crew access arm axis coordinate system)
C_Y	=	side force coefficient (missile axis coordinate system)
D	=	diameter, ft, in.
dt	=	time step, s
dt^*	=	nondimensional time step
h	=	distance of a vehicle above the launch platform, ft
h/L	=	vehicle liftoff ratio
L	=	tower height, ft
L_{ref}	=	reference length, in.
ll	=	lineload
lm	=	line moment
$\hat{n}$	=	unit normal vector
Q	=	Q criterion, where $Q \equiv (\omega^2 - S^2)/2$
Re_D	=	Reynolds number based on core diameter
$\boldsymbol{r}$	=	moment arm vector
S	=	rate of strain, 1/s
u	=	velocity, ft/s
x	=	Cartesian coordinate parallel to longitudinal centerbody axis
y	=	Cartesian coordinate orthogonal to longitudinal centerbody axis and pointed toward the solid rocket boosters
y^+	=	dimensionless wall distance
z	=	Cartesian coordinate orthogonal to longitudinal centerbody axis and solid rocket boosters (completes the right-hand rule); elevation from the ground, ft
α	=	angle of attack (wind axis coordinate system), deg
α_P	=	total angle of attack (missile axis coordinate system), deg
β	=	sideslip angle (wind axis coordinate system), deg
Δ	=	difference
$\Delta C_A/(\Delta x/L)$	=	nondimensional axial force lineload coefficient
$\Delta C_N/(\Delta x/L)$	=	nondimensional normal force lineload coefficient
$\Delta C_Y/(\Delta x/L)$	=	nondimensional side force lineload coefficient
γ	=	crew access arm deployment angle, deg
Θ	=	relative wind angle, deg
θ	=	hatch deployment angle, deg
$\boldsymbol{\sigma}$	=	stress tensor
τ	=	time
ϕ	=	body circumferential angle (body axis coordinate system), deg
ϕ_{azi}	=	freestream wind azimuth angle, deg
ϕ_P	=	roll angle (missile axis coordinate system), deg
ω	=	vorticity

Subscripts

avg	=	average value
centerbody	=	relating to entire portion of a rocket, including the core and anything above the core
core	=	relating to the vehicle core (center stack below the launch vehicle stage adapter)
inst	=	instantaneous value
norm	=	normalized value
port	=	relating to the port solid rocket booster
star	=	relating to the starboard solid rocket booster

Presented as Paper 2023-0236 at the 2023 AIAA SciTech Forum, National Harbor, MD, January 23–27, 2023; received 18 July 2023; revision received 15 November 2023; accepted for publication 14 December 2023; published online 3 April 2024.

*Lead SLS CFD Aerodynamics Research Engineer, Configuration Aerodynamics Branch. Senior Member AIAA.

†Aerodynamics Research Engineer, Configuration Aerodynamics Branch. Senior Member AIAA.

‡Aerodynamics Research Engineer, Configuration Aerodynamics Branch.

§Aerodynamics Research Engineer, Configuration Aerodynamics Branch. Member AIAA.

¶Former Aerodynamics Research Engineer, Configuration Aerodynamics Branch. Associate Fellow AIAA.

I. Introduction

THE NASA Artemis program is a large-scale program that seeks to enable human-class deep-space exploration. Most of the Artemis program is supported by NASA with contributors from 15 unique NASA sites. In addition to key NASA/industry partnerships, several international organizations provide support to the program. A number of missions, both crew and cargo, are planned to develop the infrastructure and equipment necessary for sustained human presence on the moon. A family of heavy-lift vehicles, the Space Launch System (SLS), delivers individuals and equipment to the moon. Mounted atop a crewed vehicle, the four-astronaut Orion capsule, with an endurance of 21 days, will ferry astronauts to and from the moon.

A. Space Launch System

The SLS is a central element of the Artemis program that provides the capabilities required for manned deep-space exploration. As currently planned, this family of heavy-lift vehicles will enable the exploration of the moon and Mars [1–6]. Three classes of the SLS configuration, each of which includes both a crew and cargo version, are part of the family plan. From smallest to largest, the vehicles include Block 1, Block 1B, and Block 2. A common core for all vehicles holds the fuel for four RS-25 engines that produce a total of 1.7 million pounds of thrust. Mounted on the side of the core, two five-segment single-use solid rocket boosters (SRBs) each yield approximately 3.6 million pounds of thrust such that the desired mission profile can be achieved. The payload, whether the Orion crew capsule or cargo compartment, is mounted atop the rocket.

Throughout the course of a flight, to the SLS program is exposed to a wide variety of flight regimes through the mission profile. While on the launch pad and during the early portions of liftoff, the rocket is subjected to low-speed flow with ground winds from any direction. Immediately after launch, the vehicle enters the liftoff and transition phase of flight with low subsonic Mach numbers and large angles of attack. Ultimately, the rocket leaves the liftoff and transition phase and enters the ascent phase, in which it experiences subsonic, transonic, and high supersonic flight regimes. The work in this study, which captures computational work at the NASA Langley Research Center (LaRC), was focused on the prelaunch as well as the liftoff and transition flight regimes, in which the vehicle was stationary on the launch pad through launch and up to a vehicle speed of Mach 0.3.

B. Coordinate Systems

The baseline coordinate system, referred to as the Space Launch System structural coordinate system and defined in SLS-SPEC-048, was used for these analyses [7]. As plotted in Fig. 1a, the x axis is pointed down the centerline of the body, and the y axis is orthogonal to the vehicle centerline and points toward the starboard, or right, SRB. The orientation of z completes the right-hand rule. In addition, the body circumferential angle ϕ is defined in Fig. 1b [8]. As depicted, the freestream velocity is aligned with the z axis such that the system tunnel is on the windward side of the vehicle for ϕ of 0 deg. The moment reference point for the SLS is also shown near the base of the core. This coordinate system is used across the whole SLS program, in addition to standards at LaRC.

C. Liftoff and Transition in Free Air

Significant computational efforts and detailed analyses have been performed on the Block 1 Crew, Block 1 Cargo, Block 1B Crew, and Block 1B Cargo vehicles [6,9–18]. These analyses included both the prelaunch as well as the liftoff and transition phases of flight. During these portions of the mission, the total angle of attack α_P ranges from 90 deg at the beginning of the phase to nearly 0 deg at the beginning of ascent (i.e., Mach 0.3). The roll angle during the liftoff and transition phase ranges from 0 to 360 deg. At the moderate to large α_P usually experienced during liftoff and transition in free air ($\alpha_P > 20$ deg), significant separation is observed on the leeward side of the rocket. The wake in this region is extremely unsteady, and large-scale separation dominates the flowfield. Because of the complex flowfield, it can be difficult to accurately capture this wake using computational methods that use traditional computational schemes.

1. *Large-Scale Flowfield Separation*

Because of the high-α_P flowfield, significant separation is present on the leeward side of the vehicle. This massively separated wake, originating from separation over the SRBs and centerbody, exhibits significant unsteadiness for a large distance downstream of the vehicle. The wake, quantified by ω, downstream of an SLS-type vehicle is shown in Fig. 2. A dual-mesh approach was used to compute the flowfield in which a nearbody unstructured grid resolved the flow in immediate proximity to the body with an overset Cartesian offbody grid in the outer domain. For this configuration, the offbody grid was refined a large distance downstream, which allowed the small-scale features to be visualized through the wake. This simulation was executed at a freestream Reynolds number based on a core diameter of 600,000, $\alpha_P = 50$ deg, and $\phi_P = 0$ deg. Although broadband separation is evident for this simulation, it is possible that the wake exhibits different topological flow features at lower or higher Reynolds numbers.

2. *Asymmetric Vortex*

Vehicles with slender forebodies, such as the SLS, can generate two large, stable asymmetric vortices at moderate to high α_P

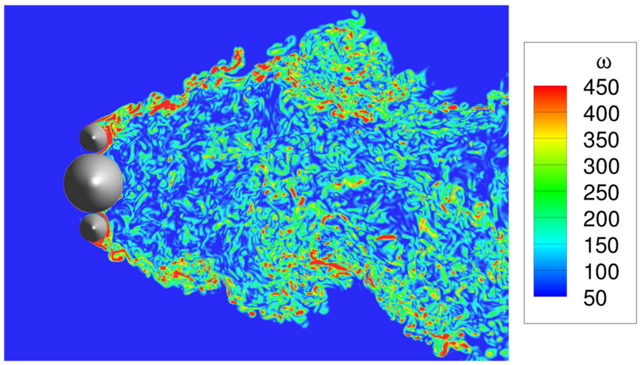

Fig. 2 Unsteady, separated wake downstream of an SLS-like vehicle, from Ref. [6].

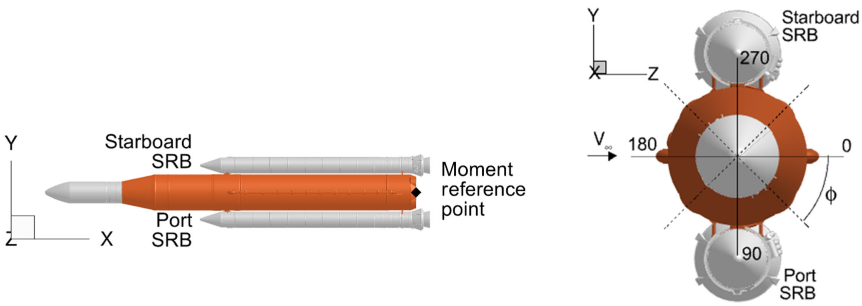

a) Side view **b) Front view**

Fig. 1 SLS structural coordinate system showing core and SRBs in a) side view and b) front view depicting body circumferential angle ϕ and freestream velocity vector, from Ref. [6].

($20 < \alpha_P < 70$ deg), as extensively documented in the literature [17,19–27]. Typically, the vortex on one side of the body will be small and stay close to the body, whereas the opposite vortex will be larger and further off the surface, as shown in Fig. 3. Both primary vortices can generate a secondary vortex, as shown in the figure. Despite the unsteady nature of the wake over a part of the rocket, these vortices vary little with time. Because of the asymmetric nature of the flowfield, a significant side force may be exerted on the body. It was observed through wind-tunnel testing that this asymmetric vortex may switch from one side of the body to the other at different instances of the same condition. With an increased downstream distance, the vortices either experience vortex breakdown or simply decompose into a massively separated flowfield. The point at which a vortex devolves is dependent on many factors, including freestream conditions, construction of the vehicle or model, and fidelity of the computational simulation. Even with high-fidelity computational solvers, it can be extremely difficult to accurately predict the asymmetric vortex because a stable state exists with the largest vortex on either side of the slender body. The schematic in Fig. 3 is from the Block 1 Cargo vehicle, in which a seam is present on the cargo fairing. Although the seam does not exist in other configurations, a similar asymmetric vortex formation can occur.

3. *Representative SLS Forebody Flowfields*

As an asymmetric vortex can form at moderate angles of attack, it is prudent to discuss a representative flowfield for an SLS vehicle. Figure 4 depicts the instantaneous flowfield around the forebody of the SLS Block 1 Cargo vehicle for $\alpha_P = 50$ deg and $\phi_P = 0$ deg. In the figure, an isosurface of constant total pressure is shown in gray with body station slices of vorticity blanked below a certain threshold, such that the vortex cores can be easily visualized. As shown in the figure and demonstrated previously for the SLS vehicle, the asymmetric vortex near the forward end of the vehicle is quite stable, with minimal temporal variations in the structure [15,16,21]. In this image, the starboard vortex is observed to lift off the surface and out of the boundary layer while maintaining a clear, well-defined vortex core as it departs from the surface of the vehicle. The port vortex remains intact until it eventually devolves into the separated flowfield. In both vortices, a vortex sheet was observed to be entrained from the windward side of the vehicle.

The flowfield presented in Fig. 4 is for one vehicle at one freestream condition. The flowfield features are known to be dependent on both the vehicle geometry and freestream conditions, especially the total angle of attack, roll angle, and Reynolds number. At moderate α_P, the forebody geometry of a cargo vehicle leads to clean, well-defined asymmetric vortices. However, this is not the case with a crew vehicle, in which the launch abort system (LAS) near the front of the vehicle disturbs the flowfield such that clean, well-behaved vortices are not present. This behavior is seen in Fig. 5a, in which the Block 1 Crew vehicle was simulated at $\alpha_P = 50$ deg, the same as the Block 1 Cargo (Fig. 4). In this figure, two asymmetric vortices form over the extreme forward portion of the LAS. The starboard asymmetric vortex lifts off the surface and devolves in a short distance. However, the port asymmetric vortex, albeit small, remains intact for a large distance off the surface. Contrary to the Block 1 Cargo rocket shown in Fig. 4, the asymmetric vortices on the Block 1 Crew vehicle are smaller than the cargo vehicle because these vortices depart from the surface on the upper portion of the LAS and do not extend over the upper stage or to the launch vehicle stage adapter (LVSA). The flow over the Block 1 Cargo vehicle at an angle of attack of 90 deg is shown in Fig. 5b, such that the flow is from the bottom of the page

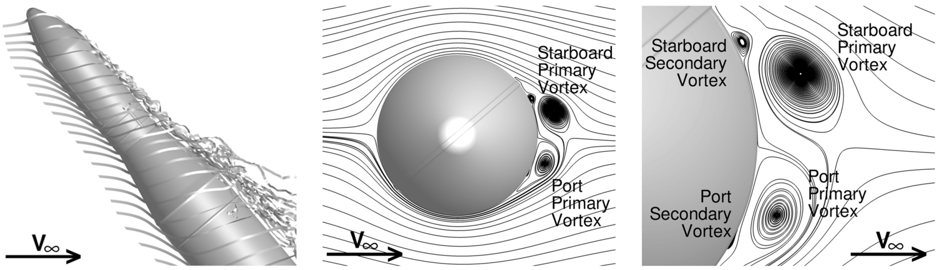

a) Profile view **b) Top down (wide) view** **c) Top down (zoomed) view**

Fig. 3 Separated flowfield showing primary and secondary asymmetric vortices in a) profile, b) top down (wide), and c) top down (zoomed) views, from Ref. [15].

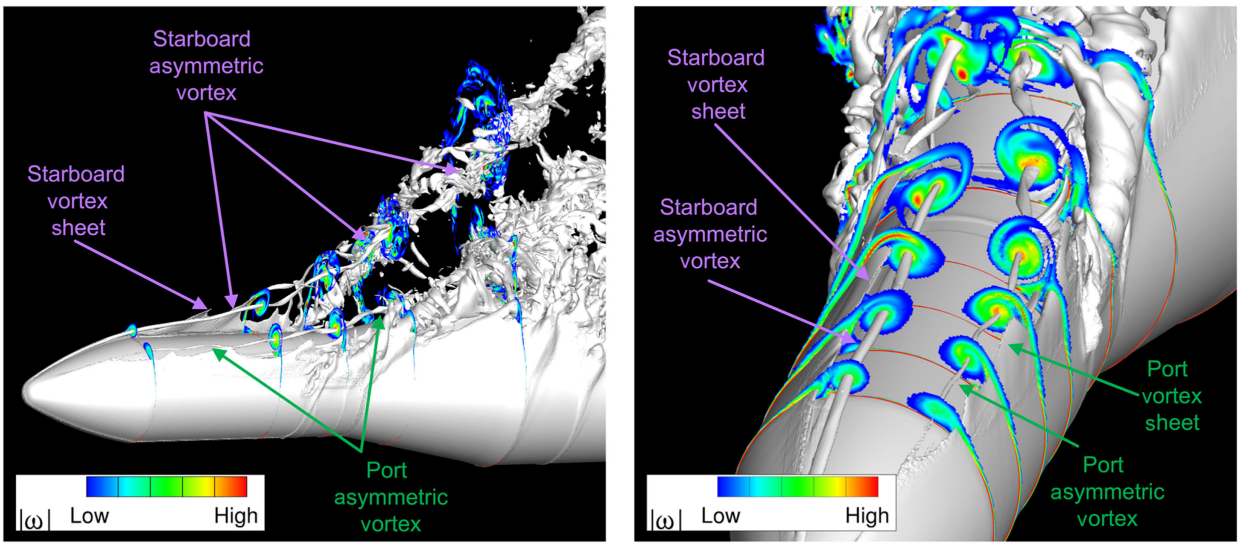

a) Wide view **b) Zoomed view**

Fig. 4 Forebody flowfield on the SLS Block 1 Cargo at $\alpha_P = 50$ deg showing a) wide view of asymmetric formation and dissipation of asymmetric vortices and b) zoomed view of asymmetric vortex formation.

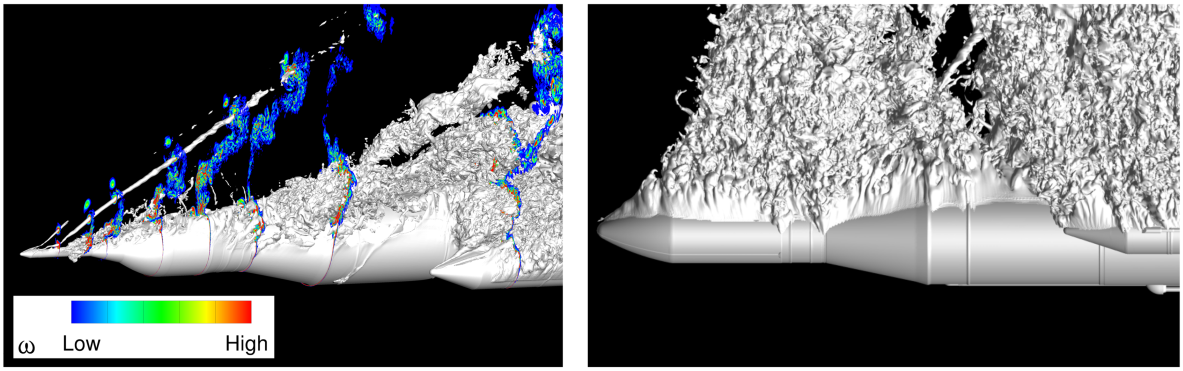

a) Block 1 crew vehicle

b) Block 1 cargo vehicle

Fig. 5 Forebody flowfield on the SLS a) Block 1 Crew at $\alpha_P = 50$ deg and b) Block 1 Cargo at $\alpha_P = 90$ deg.

toward the top. Topologically, the flowfield looks quite different than that in Fig. 4. At 90 deg, no asymmetric vortices are observed. Instead, a large, separated wake is seen to exist over the entire vehicle.

4. *Coanda Effect*

In addition to smooth-surface separation, the flow behind the SRBs is further complicated by the complex flow through the gaps between the SRBs and the core. As documented in the literature, this region can be subjected to the presence of the Coanda effect, which is the tendency of the flow emanating from a jet to remain attached to a curved surface longer than when the surface is in isolation [15,18,19,21,28,29]. The Coanda effect is particularly prominent when the rocket is sitting on the launch pad or in the early portions of liftoff/transition because it is a high-α_P phenomenon. With slight changes in the freestream condition or geometry, the flow may exhibit different attachment characteristics through the SRB/core gaps.

While the asymmetric vortices can dominate the flowfield at moderate angles of attack, the Coanda effect is most prominent at very high angles of attack. The gaps between the SRBs and the core accelerate the flow in the same manner as a jet around the highly curved surface of the SRBs and the core. Consequently, the vehicle is subjected to the Coanda effect. For the SLS, the Coanda effect is a function of the gap size between the SRBs and the core, as well as the diameter of the bodies. It has been shown that with slight changes in freestream condition or geometry, the flow may exhibit different attachment characteristics through the SRB/core gaps. Similar to the asymmetric vortices, this feature can be difficult to capture computationally, thus adding to the uncertainty of the simulations. For the case at α_P of 90 deg and roll angle of 0 deg, there are four potential different Coanda modes, as shown in Fig. 6:

1) The flow bends to the left and attaches to the port SRB and starboard side of the centerbody (Fig. 6a).

2) The flow bends to the right and attaches to the starboard SRB and port side of the centerbody (Fig. 6b).

3) The flow bends around and attaches to both sides of the centerbody (Fig. 6c).

4) The flow bends around and attaches to both SRBs (Fig. 6d).

As indicated by the vector, the freestream flow vector points to the bottom of the page. Although the figure shows the possible Coanda states at a roll angle of 0 deg, more variations exist for nonzero roll angles. For example, roll angles near 90 deg yield flowfields with minimal flow through either of the two SRB/core gaps. However, a roll angle of approximately 60 deg yields some flow through the windward SRB gap but minimal flow through the leeward SRB gap, which is in the separated wake behind the core. Because of the multiple combinations, the Coanda effect can add significant uncertainty to the numerical simulation.

All four Coanda modes are valid, stable, aerodynamic states; therefore, it is possible to computationally capture different states. This behavior is visualized in Fig. 7, as the flowfield depicts three different Coanda states. In the figure, the freestream flow points toward the top of the page. This image depicts the effect of the turbulence model on the flowfield. In this figure, the standard Spalart–Allmaras (SA) model yields flow attached to the port side of the vehicle. The addition of the rotation/curvature correction (RC) causes flow attachment to the centerbody, whereas the modified delayed detached-eddy simulation (MDDES) model causes the flow to be attached to both SRBs.

D. Liftoff and Transition in Proximity of the Tower

In addition to the complex aerodynamic features and considerations discussed in Sec. I.C, the addition of a launch tower yields more complications. The coupled effect between the vehicle and tower significantly affects not only the flowfield but also the vehicle integrated aerodynamic force and moment quantities. A high-fidelity computational model was constructed, in which the major topological features were retained but the detailed complexities were simplified [15,21]. Computational outer mold lines (OMLs) do not include every small protuberance on the vehicle, but they maintain many small features, such as cameras, latches, brackets, and feed lines. Additionally, while the computational fluid dynamics (CFD) model does not include all the fine-scale details of the true mobile launcher, the key features of the tower were retained. These features include the skeleton of the support structure, elevator shaft, and equipment rooms.

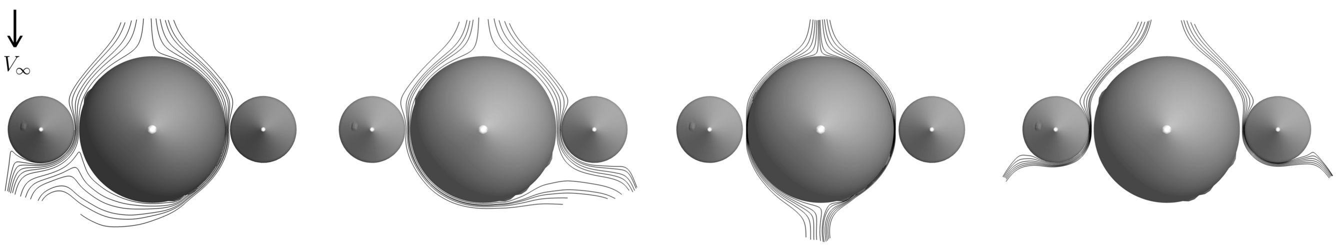

a) Flow attached to the port SRB and core

b) Flowattached to the starboard SRB and core

c) Flow attached to both sides of the core

d) flow attached to both SRBs

Fig. 6 Four different Coanda modes depicting flow attached to a) port SRB and starboard side of centerbody, b) starboard SRB and port side of centerbody, c) both sides of centerbody, and d) both SRBs.

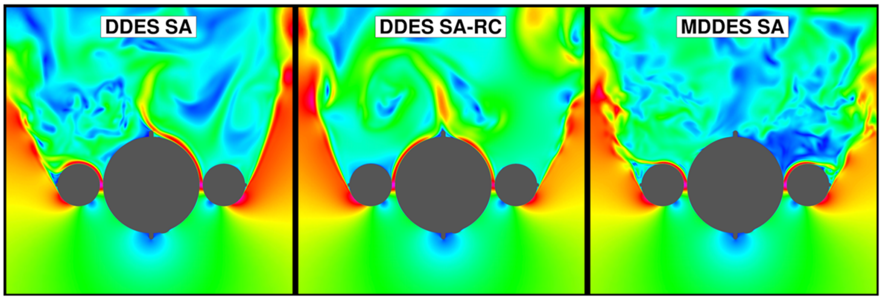

Fig. 7 Solutions with three turbulence models exhibiting different Coanda states.

During the prelaunch and also the early portions of the liftoff and transition flight segments, the location of the vehicle ranges from h/L values, the nondimensional vehicle liftoff ratio, of 0–1.5, in which $h/L = 0.0$ corresponds to the vehicle on the pad and $h/L = 1.0$ indicates that the nozzle exit plane is at the top of the tower. Although the vehicle clears the tower by $h/L = 1.0$, significant tower effects are present as high as $h/L = 1.5$. Consequently, to ensure that the aerodynamics of the vehicle in the presence of the tower was accurately captured, databases with the launch tower were generated up to $h/L = 1.5$.

Computational simulations for flight in proximity to the tower are complex due to the large wakes on the leeward side of the vehicle and tower [17,27,30–33]. It has been shown that these large wakes are insufficiently captured using Reynolds-averaged Navier–Stokes (RANS) schemes [15,16,19,21]. Consequently, it is necessary to implement scale-resolving methods such as large-eddy simulation (LES) or detached-eddy simulation (DES), a hybrid RANS/LES method. In each of these approaches, regions of fine grid density permit the appropriate modeling of both small- and large-scale flow features. Although a fine grid is desired such that small-scale eddies can be captured, database-level analysis of fine-grid solutions may be impractical. Consequently, the use of adaptive mesh refinement can be implemented to capture flowfield gradients both close to the vehicle and in the wake.

II. Program Needs

Support for the Artemis program and the SLS requires advanced aerodynamic analysis using both experimental and computational methods. The main users of aerodynamic data are the Structural Loads and Dynamics and Guidance, Navigation, and Control groups. A summary of program requests is discussed in this section.

A. Computational Challenges

The computational databases for low-speed liftoff and transition SLS calculations are complicated because of numerous considerations. To ensure the integrity of the computational results, methods must be employed that capture sufficient geometric details, accurately calculate the flowfield, and are simulated at a sufficient number of conditions to yield a high-quality database. Each of these poses independent complications, as shown in the schematic in Fig. 8. With each successive overlap between ovals, the computational problem yields additional complications. The SLS liftoff and transition Improved Delayed Detached-Eddy Simulation (IDDES) database work, shown in shaded green in the middle of the figure, is particularly challenging. Extensive experimental and computational efforts, both historical and current, have been undertaken in an effort to accurately capture the requisite liftoff and transition data [3,6,8,15–22,27,30–32,34,35].

B. Databases

Aerodynamic support for the SLS requires the use of both wind-tunnel tests and computational simulations to develop aerodynamic databases across the flight mission profile. Because of the wide range of flight conditions experienced during the trajectory of a flight, numerous tools are required to accurately capture the properties of the complex flowfields that evolve over time. Experimental results, which are useful and necessary, are essential for the construction of

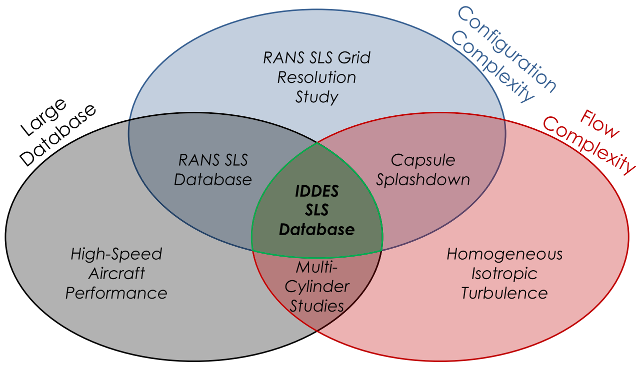

Fig. 8 Venn diagram capturing challenges to various computational applications, inspired by Ref. [15].

databases and validation of computational results. These computational simulations yield results at flight conditions that are not easily tested in a wind-tunnel facility. In addition, the computational flowfield can be easily interrogated on the surface and in the volume, thus revealing fine-scale details that are not measurable or at least not easily measured in a wind tunnel.

Databases of aerodynamic forces and moments acting on the vehicle throughout the flight regime are provided to several different SLS subteams, with the most prominent being the Loads and Guidance, Navigation, and Control groups. Although integrated forces and moments on the different components of the vehicle are captured in both computations and experiments, it is not easy to measure distributed loads in an experimental environment. The longitudinal load distribution, referred to as the lineload, is of particular interest [8,15,16, 19–21,35–38]. Complex pressure-sensitive paint (PSP) experiments for low-speed flows are not possible with the current state-of-the-art methods. In addition, PSP does not capture the skin-friction coefficient C_f distribution, which is a contributing factor to the lineloads. Because of the limitations of PSP experiments, computational simulations serve a vital purpose in generating these lineload data.

C. Mobile Launcher

The Mobile Launcher is a ground structure used to assemble, process, transport, and launch the SLS rocket and Orion spacecraft. This system comprises a crawler–transporter and a launch tower, as shown in Fig. 9a. On the Mobile Launcher, many umbilicals provide power, communication, coolant, propellants, and stabilization of the SLS before vehicle launch. Construction of the SLS is done inside the large Vehicle Assembly Building (VAB). The Mobile Launcher slowly crawls from the VAB to the NASA Kennedy Space Center Launch Complex 39B, a journey of 4.5 miles that takes approximately 8 h, as shown in Fig. 9b. The Mobile Launcher with the SLS is subsequently lowered onto the launch pad, and the crawler–transporter moves safely away from the launch pad before launch. The majority of the systems needed to launch the SLS are integrated into the Mobile Launcher because minimal infrastructure exists at the launch pad.

a) Ground view of Mobile Launcher b) Aerial view of Mobile Launcher

Fig. 9 Mobile Launcher, including both a) ground and b) aerial views. (Photographs: NASA)

D. Atmospheric Boundary Layer

Most simulations in this project were executed under uniform freestream conditions, which closely approximate the boundary conditions imposed in a wind-tunnel test. However, in actuality, the vehicle is subject to an atmospheric boundary layer when the rocket is in close proximity to the ground. This boundary layer, which may be hundreds of feet tall, can have a significant effect on the SLS configuration, which is also hundreds of feet tall. The vehicle is subject to an atmospheric boundary layer when the vehicle is static on the launch pad and for a short time after the rocket clears the tower. Databases provided to the SLS program include data with differing vehicle geometries, tower geometries, vehicle heights relative to the tower, angles of attack, roll angles, freestream velocities, and Reynolds numbers. In general, simplifications and assumptions of the database structure have been made such that computational resources are not excessive relative to the fidelity of data that is required. The data from these efforts help augment the databases with a constant-velocity profile to a database, which is subject to an atmospheric boundary-layer profile. In addition, the information informs the uncertainty of the Ground Force Loads databases.

E. Crew Access Arm

Access from the tower to the vehicle is provided by the crew access arm (CAA). Located near the top of the launch tower, the CAA can deploy and retract to provide astronaut and support crew access to the vehicle. Approximately 1 h before launch, the CAA retracts into the proximity of the tower. Two photographs of the CAA, in both the stowed and deployed configurations, are shown in Fig. 10. Emergency egress procedures require that the CAA can serve astronaut egress in a wide range of conditions. In addition to exhibiting favorable and stable behavior in the deployed position, the CAA must be able to deploy from the tower to the vehicle in no more than 45 s. Consequently, the coupled effects of the tower, CAA, and rocket must all be considered simultaneously. As the safety of astronauts is of utmost importance, detailed CFD analysis of the CAA is necessary to ensure a robust design of the system in the presence of wind at a variety of speeds and from any direction.

F. LAS Hatch

In addition to aerodynamic databases for the standard configuration, CFD simulations were executed to develop aerodynamic loading databases in support of emergency egress analysis for the Orion program. Two access hatches exist on the vehicle: an Orion hatch and a LAS hatch. An opening mechanism couples the Orion hatch to the LAS hatch, such that the Orion hatch pushes on the LAS hatch when opening. The LAS hatch must be able to deploy from a fully closed position to a fully deployed position in less than a specified amount of time under a given load limit. Figure 11 shows a photograph and CAD representation of the system. This work is critically important to ensure the safety of the crew during an emergency event, in which the crew must exit the vehicle on the launch pad.

III. CFD Tools

Analyses of the complex flowfield surrounding the SLS vehicle require numerous tools to both calculate the flowfield and postprocess these data to provide information to other groups supporting the SLS program. In particular, the massively separated wakes at large α_P

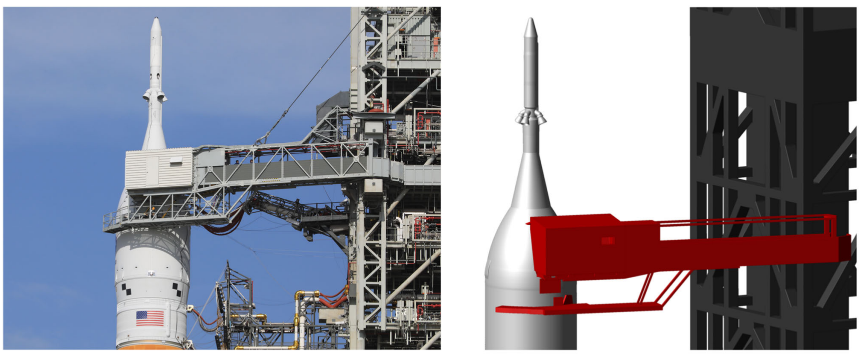

a) Deployed crew access arm b) CFD model of deployed crew access arm

Fig. 10 Crew access arm on launch tower a) in deployed position and b) computational loft. (Photographs: NASA)

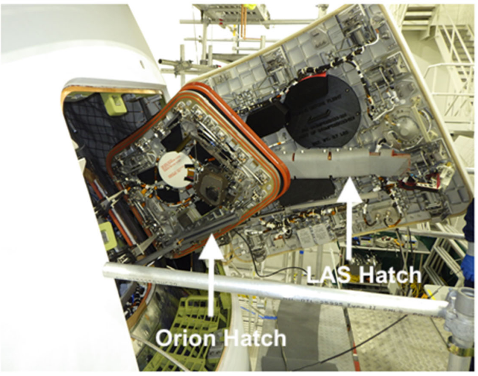

a) Photograph of the Orion and LAS hatches

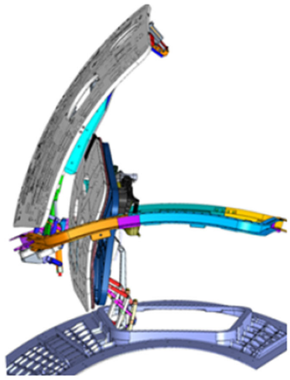

(b) CAD model of the Orion and LAS hatches

Fig. 11 Orion and LAS hatches showing a) a photograph and b) a CAD model. (Photographs: NASA)

must be calculated with complex, unsteady computational solvers using large-scale high-performance computing tools. Because database level analyses are performed on the vehicle, both integrated loads and load distributions are calculated and delivered. An overview of these tools is presented in this section.

A. Uncertainty Sources

A myriad of uncertainty sources manifest within this, as any, computational framework. A combination of mitigation and quantification of these uncertainties comprises the current state of practice for SLS computational data generation. In general, the CFD framework can be organized into four very broad steps: 1) geometry simplification, 2) grid generation, 3) solution setup and iteration, and 4) solution reporting. Within each of these steps, multiple factors contribute to the resultant quantities of interest, which differ from those experienced by the real vehicle.

The most significant source of uncertainty during geometry simplification is the removal of features deemed too complicated to model and not significant enough to retain. This practice requires a great deal of engineering expertise; information gleaned from data taken throughout the iterative design process informs the estimated significance (or lack thereof) of different features, which can change significantly as the vehicle configuration evolves. In general, any surface feature smaller than the accepted grid scale is removed; other larger structures may undergo simplification but not outright removal, as is the case with booster attachment hardware.

The generated grid structure can be broadly split into three components: surface grid, nearbody grid, and offbody grid. The surface grid uncertainty lies primarily in the selected resolution of small features, but other factors, such as artificial surface roughness, must also be accounted for. Likewise, the nearbody grid can greatly influence the resulting quantities of interest based on the height of the initial cell layer, layer growth rate, and total number of layers. The nearbody grid is often structurally different from the offbody grid and often less adaptable during a simulation. The offbody grid determines crucial aspects, such as how well the wake is resolved and how far downstream convecting structures can propagate. In Kestrel, the offbody grid is adaptively refined via flow gradient criteria; this adaptive refinement adds an additional layer of complexity to the grid generation-propagated uncertainty. Grid resolution studies and comparison with other data sources are the current best practices by which grid generation uncertainty is addressed. Section IV.A discusses the grid generation procedure in more detail.

The form of the flow solution is perhaps the most significant source of variation within the computational framework, but this does not necessarily translate to it being the largest source of uncertainty. Although a computationalist can adjust numerous aspects of the simulation (e.g., the formulation itself, time accuracy, iteration resolution, compressibility limiters, derivative schemes, subgrid and turbulence modeling choices, and relaxation factors), there are regular flow prediction workshops and rigorous internal reviews, which establish and monitor recommendations for how to assign these parameters such that they do not confound the final answer or its fidelity. Section IV.D presents examples of how even different versions of the same CFD code can present different final averaged values. In the context of SLS CFD, certain more case-specific uncertainty sources require more specific attention (e.g., whether the engine plumes affect the aerodynamics enough to be modeled and whether the freestream wind profile can be uniform when simulating the rocket and tower before liftoff). Discussing these sources in detail is beyond the scope of this paper, but they are nuanced and active areas of research.

There is also uncertainty introduced as computationalists reduce their flow simulations to tabulated quantities of interest. If the flow is simulated to be time accurate, then the delivered value can differ based on the number of preliminary iterations that are performed, as well as how large the averaging window is set to be. Solution convergence criteria can vary from code to code and from application to application. Furthermore, if the flow exhibits multistable flow states, it is not always clear how those states can be reconciled into a single datum or which state should be solely represented in the delivered database. Again, the CFD community has endeavored to establish norms by which these types of decisions are made. In the SLS program, the presentation of multistable states has even altered the structure of the delivered data to ensure that the physics is most reasonably communicated and database users have access to the likely gamut of flow physics experienced by the rocket.

B. USM3D

Over the course of the SLS program, computational methods have been regularly developed and refined. The earliest SLS simulations were executed using USM3D, a CFD code developed by the Configuration Aerodynamics Branch of NASA Langley Research Center. USM3D is an unstructured, cell-centered, finite volume scheme that can be used to solve both Euler and Navier–Stokes equations. At the time of the investigation, this code had both RANS and DES models. The best practices that had been developed previously for ascent analysis during the Ares program were applied to the SLS analysis in the transition flight regime [39,40]. In the ascent flight regime, standard RANS schemes can be adequately used, whereas massive separation in the transition flight regime requires an unsteady solver. The methods employed for DES simulations were investigated using both a circular cylinder and a simplified Titan III launch vehicle [19]. Unstructured grids were developed using VGRID meshing software with increased refinement near surface protuberances and in the wake of the vehicle [21]. To adequately resolve near-body and off-body flowfield structures, a DES grid requires an increased grid density in the wake, whereas a RANS grid does not.

While unsteady simulations never approach typical convergence criteria, time averaging can be applied once the simulation has been properly set up and reaches a statistically steady state. The computational data collected at $\phi = 0$ deg are compared to an experimental

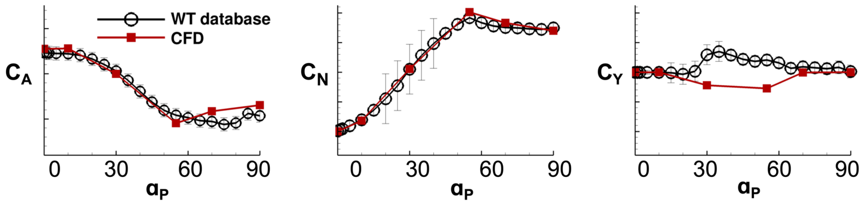

a) C_A b) C_N c) C_Y

Fig. 12 Integrated force and moment coefficients from wind-tunnel database and DES k–ϵ USM3D simulations.

database shown in Fig. 12, in which the experimental data were collected in the 14- by 22-Foot Subsonic Wind Tunnel (14×22) of NASA Langley Research Center [19]. As shown in the figure, good agreement is observed in the normal force coefficient, which is the largest coefficient for this freestream condition. Despite the good agreement, the simulations took approximately 5 days on 1200 processors to complete the time-averaging window. In addition, as adaptive mesh refinement was not available in USM3D, different grids were made for various combinations of α_P and ϕ. For these two reasons, it was desirable to investigate other solvers to determine the best tool for this analysis.

C. FUN3D

FUN3D, a CFD code developed and maintained by the Computational Aerosciences Branch at the NASA Langley Research Center, was subsequently examined. It is a node-centered code that can be used to solve both The Euler and The Navier–Stokes equations. Simulations can be executed using baseline tetrahedral grids and mixed-element unstructured grids that include tetrahedra, prisms, and pyramids. Unsteady schemes include DES, delayed detached-eddy simulation (DDES), and MDDES with both single-equation SA and numerous two-equation turbulence models. Both standard and RC SA models are available. As FUN3D is node centered, a grid with 459 million tetrahedra corresponds to only 78 million nodes. Consequently, the USM3D solutions contain approximately six times as many degrees of freedom as FUN3D for the same grid. Because of the grid generator tool limits at the time, the maximum number of grids that could be generated was 717 million cells and 122 million nodes. Consequently, this FUN3D simulation includes approximately one quarter of the cells of a similar USM3D computation. Although adaptive mesh refinement is now available in FUN3D, these schemes were not coupled with unsteady solvers at the time of tool evaluation. Consequently, grids were generated for different freestream angles.

A body station cut of surface pressure computed with FUN3D at α_P of 90 deg and ϕ of 0 deg is shown in Fig. 13 for a number of turbulence models and compared to the 14×22 data. As shown in the figure, good agreement is seen on the windward side of the vehicle, but disagreements were observed both on the leeward surface and the SRB/core gap. In an additional investigation, the SRB/core pressure differences were due to the prediction of different Coanda states [19]. Consequently, while the SA–RC solution yielded the best agreement with the 14×22 data, the other computations were valid. After the investigation, the lack of adaptive mesh refinement and requirement for extremely large grids led to the conclusion that another tool should be sought.

D. Kestrel

The Kestrel CFD package is a suite of programs that enables solution preparation, adaptive grid generation, computational calculation, and simple postprocessing of both RANS and IDDES schemes [41–44]. Kestrel is developed and maintained by the Computational Research and Engineering Acquisition Tools and Environments, Air Vehicle (CREATE-AV) project and executed by the U.S. Department of Defense High Performance Computing Modernization Program (DOD HPCMP). This software package was originally developed to support acquisition efforts that require multidisciplinary analysis of vehicles, including aerodynamics, dynamic stability and control, structures, propulsion, and store separation. A common scalable infrastructure allows for a modular approach for which different multidisciplinary analysis methods may be either coupled or decoupled from each other.

The KCFD flow solver is a finite volume, cell-centered, unstructured flow solver for both two- and three-dimensional configurations. Solutions can be executed on a variety of cell types, including tetrahedra, prisms, pyramids, and hexahedra. Parallel processing is executed by splitting the computational domain into the same number of zones as processors, and a method of lines approach is used such that the temporal and spatial integration schemes are decoupled from each other. A second-order-accurate spatial algorithm is used, and up to a second-order-accurate temporal scheme is implemented with a subiteration point-implicit algorithm. A wide number of settings can be used to control the behavior of the computational solver. Some of these values can dramatically affect the fidelity and stability of a solution; therefore, great care must be taken when setting each parameter.

In some cases, it may be necessary to accurately resolve a flowfield exhibiting separation or other complex off-body flowfield features. Although a large unstructured grid can be generated, it may be desirable to implement an adaptive mesh routine to yield a high-resolution grid, where large gradients exist while relaxing the cell size in other portions of the flowfield. If this is selected in Kestrel, a dual-mesh approach, including a static near-body unstructured grid and an adaptive off-body Cartesian grid, is employed. Similar to KCFD, SAMAir, an offbody Cartesian grid solver, is dependent on the number of parameter values chosen by the user. Unlike the user-generated unstructured grid, both the initial and final Cartesian grids are automatically generated using SAMAir. A trimmed internal unstructured grid is combined with user-specified outer boundary domain limits for the Cartesian grid. The overlap between the two grids and the associated grid density is generated by SAMAir such that the structured and unstructured cell sizes are similar at the edge of

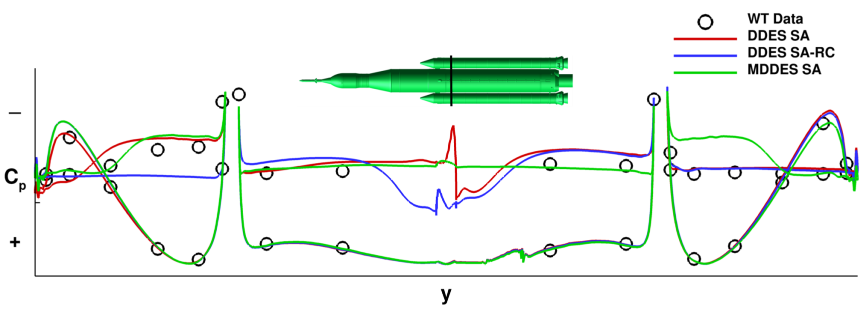

Fig. 13 Body station cuts showing surface pressure for experimental and computational data.

the inner grid. Refinement is executed at a user-specified number of iterations for a given maximum cell size, and refinement tracks one of approximately 10 metrics, such as the magnitude of vorticity ω.

E. Computational Resources

All simulations were performed on Pleiades, a large-scale Linux cluster located at the NASA Advanced Supercomputing facility at the NASA Ames Research Center. The computer consisted of 158 racks of nodes, over 11,000 nodes, over 241,000 compute cores, and nearly one petabyte of memory. Cores were connected through InfiniBand with a partial hypercube topology. Within the NAS ecosystem, a number of computational chips can be used for simulations, and most simulations were performed using the Intel Haswell, Skylake, and Cascade Lake nodes. Depending on the complexity of the simulation, most notably the presence of the tower, computations were performed anywhere from 1000 to 3400 processors resulting in jobs that took between 24 and 100 h. As a database-level analysis was performed, great care was taken to conserve disk storage space. These efforts included saving a subset of the simulation at a given time step, slices through the volume domain, or only saving the surface data. A standard job, in which only a limited volume data were saved, used approximately 600 GB of disk space.

F. GridTool

GridTool, a component of the Tetrahedral Unstructured Software System (TetrUSS) of the NASA Langley Research Center, was used to prepare the geometry for both grid generation and solution setup [45,46]. Within GridTool, surface patches defining the entire OML are defined and then grouped to form components. Patches can be defined by a single or multiple underlying surfaces. By leveraging automatic geometry programs augmented with significant user work, more than 7300 surfaces and nearly 4500 patches were used to define the surface OMLs. Patches on the OMLs are defined by many different curves that are usually but not always coincident with an underlying surface. These surfaces, most of which are nonuniform rational B splines, were systematically and carefully constructed by a small team of engineers at the NASA Langley Research Center across two different branches. Many patches were combined together to generate one component [6]. A large number of protuberances were retained over the entire vehicle. The grid density was defined based on the size and location of various sources, which must be carefully constructed to ensure that an adequate computational grid is generated. Many thousands of sources were hand placed on the geometry to specify grid sourcing throughout the vehicle, requiring significant user interaction.

G. HeldenMesh

With the maturation of the SLS program, the existence of new tools allowed for standard practices to be updated for improved workflow. HeldenTool, a geometry tool developed by Helden Aerospace, was used for both surface representation and sourcing. Similar to the functionality of GridTool, HeldenTool can be used to define surface geometry, boundary conditions, patches, and components. HeldenTool and the associated HeldenMesh use automated sourcing based on patch names, which requires minimal hand work. This automatic sourcing yielded more than 50,000 sources for the SLS Block 1 Cargo vehicle. HeldenMesh is a three-dimensional unstructured grid generator that triangulates the surface and uses the advancing-layer method to grow the viscous grid and the advancing-front method to grow the outer mesh. Within the advancing-layer technique, the viscous grid spacing is defined by

$$\delta_j = \delta_1[1 + R_1(1 + R_2)^{j-1}]^{j-1} \tag{1}$$

in which δ defines the cell spacing, j represents a grid index, δ_1 is the user-specified cell height for the first cell, and R defines two growth rate parameters [47]. As seen in the equation, the number of layers for the viscous grid cannot be specified by the user. This viscous grid continues to grow until the cell size is similar to the size generated by the source distribution.

H. Lineloads

Lineloads and line moments are a mission-critical product within the SLS design framework [48–51]. Similar to the spanwise load distributions on an airplane wing, these partially integrated surface stresses enable structural, control, and performance assessments that are not possible with only integrated vehicle force and moment information. Mathematically, lineloads and line moments are computed as integrals over a wetted surface with the exclusion of the dimension of interest. If x is that dimension, then the equations are

$$ll(x) = \oint\!\!\oint \boldsymbol{\sigma} \cdot \hat{n}\, \mathrm{d}y\, \mathrm{d}z \tag{2}$$

$$lm(x) = \oint\!\!\oint \boldsymbol{r} \times (\boldsymbol{\sigma} \cdot \hat{n})\, \mathrm{d}y\, \mathrm{d}z \tag{3}$$

in which $\boldsymbol{\sigma}$ is the stress tensor, $\hat{n}$ is the surface unit normal vector, and $\boldsymbol{r}$ is the moment arm to an arbitrarily defined reference point. In practice, lineloads are computed using a surface mesh binning procedure. A surface mesh is segregated into bins along the axis of interest (with a width of, e.g., Δx), and then the mesh is fully integrated within each bin [52]. This process yields centerline-integrated loads that retain the desired dimensional dependence. The representative lineloads of all three components (axial, side, and normal) for the SLS are shown in Fig. 14. The nondimensional distributions are indicated by $\Delta C_{A,Y,N}/(\Delta x/L)$, in which A, Y, and N are the subscripts for the specific direction of interest. Although the data in the figure are irrelevant in this methods section, it should be noted that the case was executed at $\alpha_P = 50$ deg and $\phi_P = 0$ deg. Data for the centerbody are shown in black, whereas the two SRBs are shown in red and blue for each body. Under this condition, near-constant values of the axial force coefficient lineload result from the 0 deg roll angle. The peaks of the side force coefficient lineload near the SRB noses are a result of the asymmetric vortices on these components. Finally, the normal force coefficient lineload shows a significant variation over the length of the entire launch vehicle.

I. Tecplot Chorus

Database-level analysis of computational data is a time-intensive process that requires significant postprocessing and analysis. This work, which is largely manual in nature, can be streamlined and enhanced by using software. Tecplot Chorus is a database-level management software package that can be used to organize and manage large datasets. Chorus allows the user to simultaneously visualize results from numerous simulations at the same time such that different simulations can be visualized with a few clicks of a mouse instead of tedious, somewhat cumbersome, manually sifting through data. To evaluate the effectiveness of the software, a representative database was interrogated. A catalog of Tecplot visualization templates and analysis scripts was developed to systematically

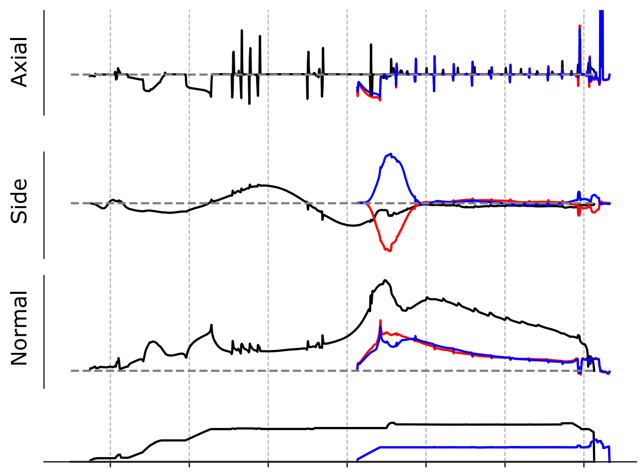

Fig. 14 Example SLS lineloads for the axial, side, and normal components of force.

extract the flow visualization and performance coefficients, all of which were visualized within Chorus.

IV. Computational Methods

With the maturation of the SLS program, the computational methods in the liftoff and transition flight regime have been developed and refined. These efforts include the development of high-quality computational grids, including both nearbody and offbody grids. Additionally, a baseline computational setup was developed and thoroughly defended through an exhaustive study by Pomeroy and Krist [15]. Finally, the effect of the Kestrel versions on the solution was systematically updated when new versions of the software were released. The information in this section includes an explanation of the current best-practice methods.

A. Grids

It is widely known that the computational mesh used in a study can have dramatic effects on the accuracy of the simulation; thus, the importance of a high-quality grid cannot be overstated. Because the Kestrel formulation employs a near-body unstructured grid overlapped with an offbody Cartesian grid, the integrity of both computational grids must be verified. Because the offbody grid is subject to adaptive mesh refinement, the integrity of the Cartesian grid must be verified under numerous freestream conditions or rocket configurations.

Before execution in Kestrel, the Carpenter tool was used to prepare the unstructured geometry before the Cartesian grid overlap. The Carpenter tool, distributed as part of the Kestrel suite from the DOD CREATE-AV HPCMP, truncates the grid at a user-specified distance off the surface of the vehicle surface. This distance, which was constant throughout the entire domain, was selected such that a sufficiently fine resolution would capture any flow separation in the wake immediately downstream of the body. Two views of the inner and outer grids are shown in Fig. 15. The static, inner, and unstructured grid is shown in gold. The Cartesian grid, shown in gray, was subjected to adaptive mesh refinement. A magnified view depicts the details of the overlap region. As visualized in the figure, the smallest cell size in the Cartesian grid, which is generated as part of the solution process, has a cell size similar to that of the outermost unstructured cell.

1. *Unstructured Inner Grid*

Grids in the early portion of the SLS program were generated in the TetrUSS grid package (VGRID) and subsequently trimmed using Carpenter at 24 in. Best practices were later updated to generate HeldenMesh grids that were trimmed to 36 in., as discussed in Refs. [6,15,19].

As mentioned previously, the unstructured surface grid was generated in HeldenMesh using methods generated over the course of the SLS program. Using the geometry defined in HeldenTool, a large number of source distributions on a variety of patch families were declared and generated using HeldenMesh. For a typical configuration, in excess of 50,000 sources were generated, resulting in approximately 1.1 million triangular surface cells, depending on the specific SLS configuration. The size and stretching ratios of these cells varied significantly across the surface of the rocket. A significant number of small-scale features were appropriately modeled. These include attachment brackets, connection hardware, camera mounts, and assorted aerodynamic fairings. Other major features include the liquid oxygen lines and systems tunnels. Some of these features are shown in Fig. 15.

The resulting surface grid, quantified by both y^+ (dimensionless wall distance) and volume of the first cell, is shown in Fig. 16 for Block 1 Cargo vehicle. The y^+ plot was generated with $\alpha_P = 50$ deg. As shown in the plot, extremely small values of y^+ were present over much of the vehicle, with some elevated values resulting near the vortices. Ideally, y^+ would be less than 0.7 at all surface locations over the entire flight envelope. However, elevated y^+ values, even in excess of 1.0, were observed over the SRB noses. Figure 16b plots the volume of the first cell over the SLS. It is clear that reduced cell sizes define small-scale features, such as circumferential rings, with wider spacing declared on the core.

2. *Initial Outer Cartesian Grid*

As mentioned previously, an adaptive offbody mesh refinement scheme was employed in the analysis. Within the adaptive mesh refinement process, the outer bounds in which the offbody grid is refined must be determined. In an ideal situation, the refinement region would extend far into the wake to capture its downstream behavior. Such computations would allow farfield analysis, such as interactions between the wake and launch pad infrastructure, to be studied. However, the cost of these simulations must also be considered when setting refinement limits. These limits must be carefully considered while the fidelity of the simulation is considered for a given computational cost, and engineering judgment must be applied to select an appropriate domain. Figure 17a presents a visual representation of a representative rocket and a specified refinement box

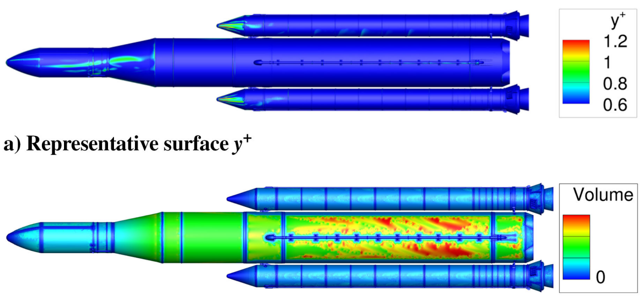

a) Representative surface y^+

b) Cell volume of the first cell

Fig. 16 Unstructured Block 1 Cargo surface grid quantified by a) y^+ and b) cell volume of the first cell.

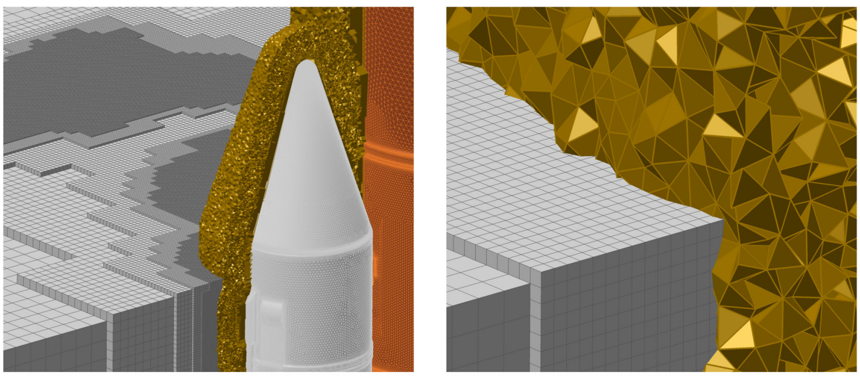

a) Wide view of grid overlap

b) Zoomed view of grid overlap

Fig. 15 Volume grid depicting unstructured nearbody grid and overset offbody Cartesian grid with a) wide view and b) zoomed view.

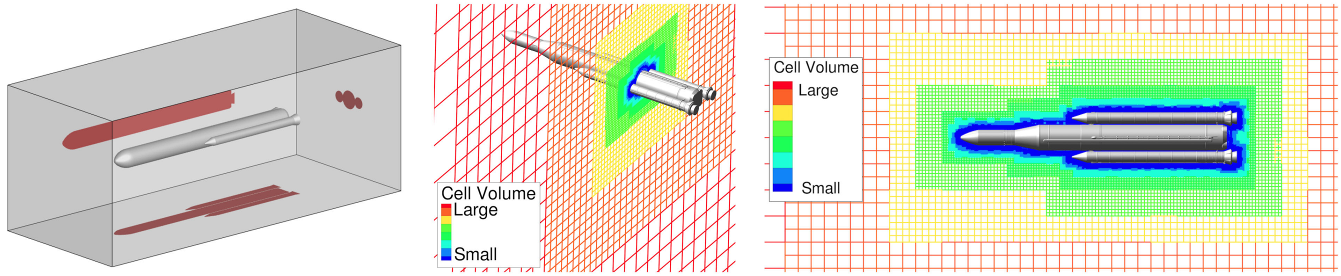

a) Off-body refinement domain b) Constant *x* slice c) Constant *z* slice

Fig. 17 Visualization of Cartesian grid a) refinement domain and slices at b) constant *x* and c) constant *z*.

region. For ease of viewing, the rocket geometry has been projected onto the *x*, *y*, and *z* planes.

Before the first iteration, or time step, was computed, an initial offbody grid was generated. This grid was later subjected to off-body refinement, but an initial grid was independent of the anticipated flowfield characteristics or any adaptive mesh refinement settings. Slices of this initial grid at a constant body station and waterline are plotted in Figs. 17b and 17c, in which the mesh is colored by the three-dimensional cell volume. The initial Cartesian grid comprised approximately 315 million nodes distributed through nearly 30,000 blocks. The inner grid extends a specified distance from the surface, whereas the Cartesian grid extends far into the outer domain.

3. *Cartesian Adaptive Mesh Refinement*

Offbody adaptive mesh refinement is applied by adding grid density in regions of high gradients in the flowfield. Because the unsteady flowfield and off-body adaptive grid affect each other, both the flowfield solution and Cartesian grid must reach a statistically steady state before either time averaging the solution or performing unsteady aerodynamic analysis. Figure 18 shows a body station cut at two different time steps, including a time step before the solution is sufficiently set up and a slice in which both the flowfield and grid are established.

For adaptive mesh refinement, the physical parameter of refinement is specified by the user as one of many selections. For the analysis in this survey paper, adaptation was applied based on the local magnitude of vorticity. In addition to the parameter upon which the solution is adapted, the sensitivity of the flowfield quantity, known as the threshold, can be determined for a simulation. The metric of interest and the sensitivity of this value to the gradients in the flowfield must be carefully selected to ensure adequate grid refinement without overresolving the flowfield. A detailed investigation by Pomeroy et al. [5,15] selected a desired threshold for such analysis. This was selected to ensure that the key flowfield features were accurately captured without yielding an unreasonable cost for the simulation.

B. Computational Setup

The baseline computational setup was similar to those used in previous studies [15,19,21,22,34,44]. Because a wide number of settings can be selected, the LaRC SLS CFD team collaborated with Kestrel developers for guidance regarding the initial selection of these input parameters. After a detailed parametric investigation, the simulation was set up to average the simulation between 5.0 and 7.0 s with a time step of 0.0005 s. The IDDES SA turbulence model was coupled with a second-order spatial and second-order Gauss–Seidel formulation and with HLLE++ inviscid flux scheme. With the exception of the IDDES model, all of these are the default settings for Kestrel.

For problems of this nature, the database requires the generation of steady-state forces and moments acting on the vehicle. Because of the unsteady nature of the flowfield, these time-dependent simulations will never converge toward steady values. Fortunately, these values fluctuate around a certain mean value after many time steps, for which the solution has set up and reached a statistically steady state. Because the time step can have a significant effect upon the fidelity and convergence of the simulation, the dimensional value must be carefully selected. The dimensional time step dt was specified as 0.0005 s. The nondimensional time step dt^*, as defined in Eq. (4) and reported to only one significant digit, was approximately

$$dt^* = \frac{V_\infty}{D_{\text{core}}} dt \approx 0.004 \tag{4}$$

In general, it is desirable to have a nondimensional time step of less than 0.01 and for the flow to not advance more than a quarter cell per dimensional time step. Based on this analysis, the lower value of the two results should be selected for the simulation. For this simulation, the flow advances by no more than a reference quarter cell per iteration, and dt^* is less than 0.01, yielding a sufficient baseline selection of dt. Similar to other parameters, the effect of this value was investigated by Pomeroy and Krist [5,15].

Numerous settings are relevant to SAMAir, the outer solver, which must be selected independently from the KCFD input values. In

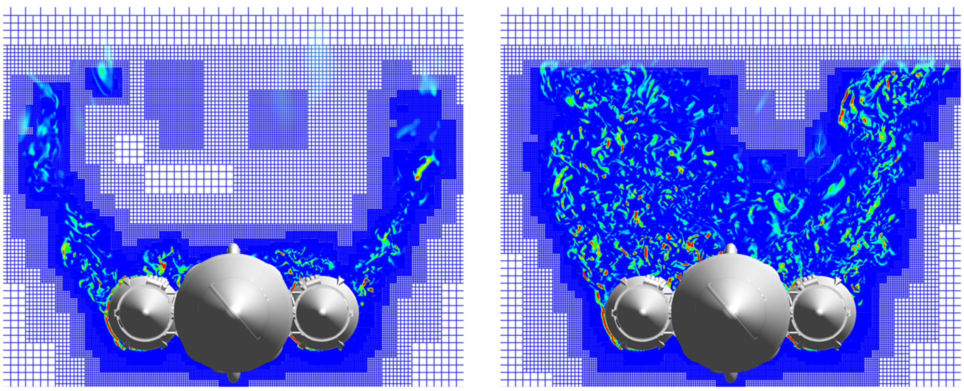

a) Grid setting up in early portion of the simulation b) Grid at the start of time averaging

Fig. 18 Adaptive mesh refinement at a) early portion of simulation and b) beginning of time averaging.

general, the same settings were used for KCFD and SAMAir. The offbody grid refinement was performed within SAMAir and commenced after the first 500 iterations. Subsequent adaptation was performed every 250 iterations, with the refinement based on ω. The refinement was performed during the entire simulation.

C. Database Postprocessing

Large-scale efforts for database construction require a large team to provide sufficient program support. With approximately 10 people supporting computational efforts at various points over the SLS program, a standard approach must be employed by all team members. In addition to the computational approach described in Sec. IV.B, postprocessing of these results was also standardized. Building upon the technology developed for the Constellation program, a new Python-driven system, which leverages both Tecplot 360 and the associated PyTecplot software, generates a standard set of plots and integrated quantities (e.g., lineloads). These standard methods ensure that all simulations performed in support of SLS can be easily compared with other cases in the database.

D. Comparison of Kestrel Versions

Because the aerodynamic support of the SLS program has spanned more than a decade, computational methods have been improved and refined with subsequent analysis. Of particular interest are the modifications made to the computational grid setup and the use of new versions of Kestrel. Meticulous checks were performed with each new major version of Kestrel to ensure the integrity of the new methods relative to the earlier versions of Kestrel. Because of the sensitive nature of these data, the results cannot be published publicly. However, the reader is assured that many internal peer-reviewed examinations have been conducted, in which the new methods and associated uncertainty were of appropriate levels.

E. Comparisons to Experimental Data

A comparison of best-practice computational data and experimental data, collected from the 14- by 22-Foot Subsonic Tunnel (14×22) at LaRC, is shown in Fig. 19, in which $\alpha_P = 50$ deg and $\phi_P = 0$ deg. The data are presented at three different body stations, as depicted in the figure. The computational data were extracted at the same points as those in the instrumented test article. Each of these circumferential points is shown with a small symbol, in which the squares and circles represent the computational and experimental results, respectively. As depicted in Fig. 1, a circumferential ϕ_P of 180 deg corresponds to the downstream-most point on the launch vehicle, which is nominally opposite the systems tunnel. The centerbody of the model was instrumented with pressure taps at seven body stations comprising 12 taps per ring. No surface taps were present on either of the SRBs because these were instrumented with force balances [8]. Overall, the two datasets showed many similarities at all the three body stations. Excellent agreement was found in both the attached and separated regions, and this observation is encouraging when considering the degree of separated flow. Small differences were observed near ϕ_P of 90 and 270 deg, which correspond to the outwardmost portion of the centerbody that forms the gap.

F. Data-Fused Reduced-Order Modeling

The liftoff and transition lineload databases are generated using a method that synthesizes both experimental and computational results. This approach, called data fusion, is used to ensure that the reported lineloads agree with experimentally measured force and moment coefficients. This procedure involves the following steps to reconcile the computationally derived lineloads with the experimentally derived integrated loads [20,53]:

1) Represent the entire collection of CFD surface dataset as a linear sum of weighted principal components, which are identified via the covariance matrix and its eigenvectors.

2) Interpolate the principal component coefficients within the parameter space to increase the number of surface solutions within the database.

3) Adjust both source and interpolated principal component coefficients as little as possible to yield an integrated (computationally sourced) surface set equal to the integrated (experimentally sourced) load set.

4) Compute lineloads from adjusted surface stresses (both pressure and skin friction) within the entire database parameter range.

5) Organize the adjusted, interpolated lineload set into the deliverable database.

This methodology allows for the delivery of lineloads throughout the parameter space that integrate to the wind tunnel-derived forces and moments, which is not possible with the original CFD solutions alone. However, as is often the case with data fusion in the experience of this group, the resulting lineloads serve as an acceptable compromise between multiple incommensurate data sources, which cannot otherwise be corrected to agree with one another.

A flowchart for database development, depicting the relationship between the experimental data and delivered database, is shown in Fig. 20. Data from an experimental test, including the integrated forces and moments and surface port pressures, are evaluated. Based on these analyses, a design of experiment method is employed to optimize the CFD run matrix. This step reduces the number of computational simulations needed for a high-fidelity database. These data are used in the development of a reduced-order model, which is based on the computational lineloads, pressure, and skin-friction distributions. Computationally derived lineloads are then augmented with the original experimental data to generate a data-fused reduced-order model, from which a lineloads database is delivered.

V. Urgent Program-Critical Support Regarding Hurricane Nicole

With contributions from many groups, significant efforts were made to reduce risk leading up to the Artemis I launch, which occurred on 16 November 2022. On 7 November, only nine days

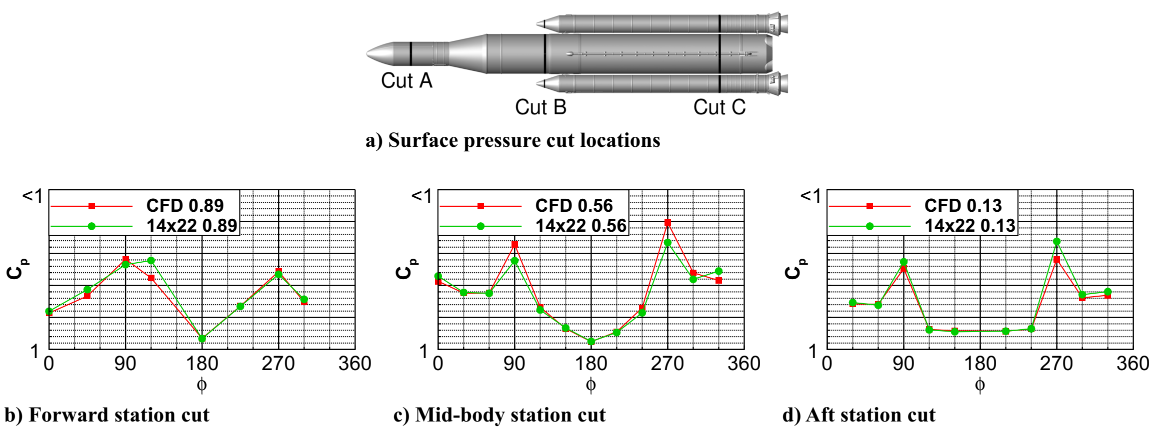

Fig. 19 Experimental 14×22 and computational pressure cuts at a) forward, b) mid-, and c) aft body stations.

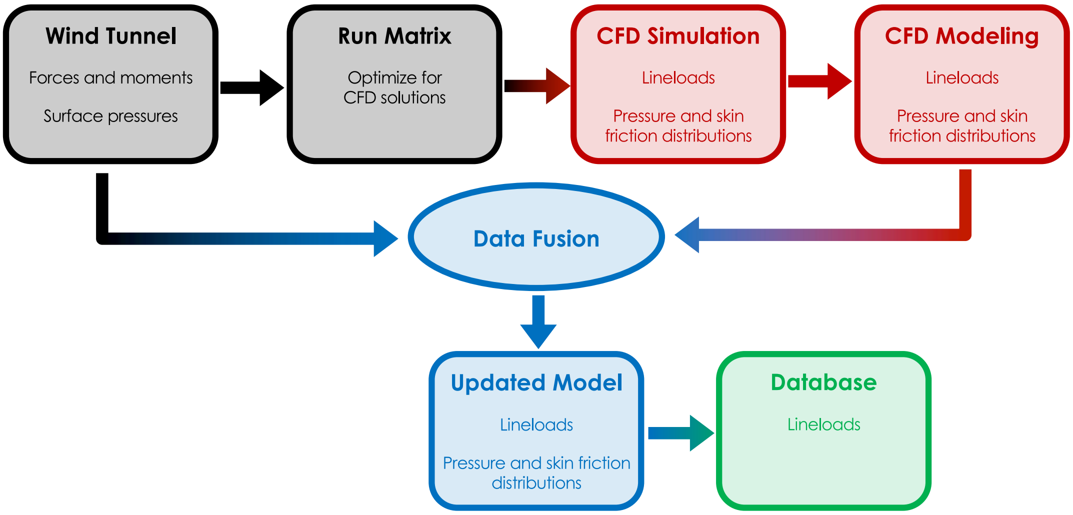

Fig. 20 Flowchart showing database generation process.

before the launch, a subtropical cyclone formed in the Atlantic Ocean south of Hispaniola. Meteorological predictions indicated that the SLS vehicle, already located on the launch pad, may be in the path of a tropical cyclone or hurricane. While the vehicle would be protected from the storm if it were rolled back to the VAB, vibration fatigue applied to the SLS during transit would add additional structural risk. However, if the vehicle were to be left on the launch pad, it may be exposed to high-velocity winds, yet not subject to as many vibrations. The aerodynamic database, supplied to the program years ago, was a key dataset that yielded the decision to leave the SLS on the launch pad and ride out the storm. Before landfall of the storm, risk reduction efforts were made across the program. This included, in part, having an unfueled rocket on the pad and turning off any excess systems on the vehicle or tower. Over time, this storm strengthened into Hurricane Nicole and made landfall into Florida. It subjected SLS to maximum winds from 3 to 5 a.m. EST on 10 November, six days before the Artemis I launch. This was partly because of the high confidence in the high-fidelity simulations, which directly contributed to the database, that the program had sufficient confidence to leave the vehicle on the launch pad. Without these computational data, the program may not have had sufficient information to safely decide whether to leave the vehicle on the launch pad.

After the storm exited the region, a detailed inspection was performed on the vehicle, and it was deemed to be structurally sound for Artemis I. However, midday on 15 November, one day before launch, it was observed that some room-temperature-vulcanizing (RTV) caulk had departed from the vehicle, which was attributed to damage from Hurricane Nicole. This is visualized in Fig. 21. Because the vehicle was damaged during the winds of the hurricane, the structural integrity of such a system during launch, with harsher conditions than those exerted by the hurricane, was questioned. On 15 November, only 14 h before the ultimate launch, the program sought guidance from the NASA Langley Research Center aerodynamics team regarding the RTV departure. Within only 2 h, the computational team was able to provide sufficient data that gave the program confidence to proceed with the launch. This was only due to high-fidelity simulations and proper archiving efforts for simulations performed five years prior that the team was able to provide the requisite data. At the time of the query, mere hours before launch, this aerodynamic effect was the single largest threat to scrubbing the launch. It is quite rare for an aerodynamics team to be urgently summoned leading up to the flight of a vehicle, whether a launch vehicle or air vehicle. For the second time in about one week, the robust computational support for the program yielded the confidence to proceed with the launch, which occurred early in the morning on 16 November with only 3 kt winds.

VI. Additional Support for the SLS Program

As discussed in Sec. II, a number of studies have been performed in support of program needs. Studies in this section could be rapidly performed using methods that had been meticulously and carefully developed for database analysis. Without these skills and tools, rapid support for the program would not have been possible. Four of these topics are presented in this section: the effect of the Mobile Launcher, analysis with an atmospheric boundary layer, and the coupled effect of the hatch and CAA. Database methods remain unchanged relative to the previously published literature [19]. All cases in this subsection were executed at Mach 0.183 and Reynolds number based on the core diameter Re_D of 615,000.

A. Mobile Launcher

The Mobile Launcher significantly affects the flow around the rocket, and the rocket also affects the flow around the tower [5,6,32]. It was desired to understand the effects of different Mobile Launcher configurations on the aerodynamics of the Block 1 Crew vehicle. Consequently, computational analyses of two MLs, namely, Mobile Launcher-1 Extended (ML-1E) and Mobile Launcher-2 (ML-2), were conducted. As documented in Ref. [5], some key simplifications were made in the computational geometry relative to the CAD program. These choices were made so that the computations could be executed with a reasonable degree of fidelity without overcomplicating the geometry or generating an unreasonable number of grid points. In particular, the CFD tower does not contain numerous systems that protrude from the production tower. In addition, the interior structure of the tower was significantly simplified. Although these two computational geometries do not capture the blockage

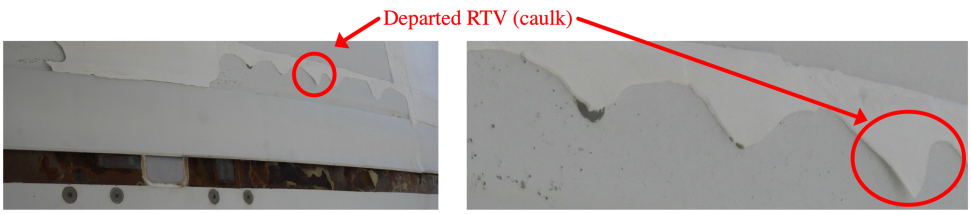

Fig. 21 Images of RTV damage to SLS resulting from Hurricane Nicole. (Photographs: NASA)

through the tower, the two towers are sufficiently similar such that the aerodynamic differences between the towers can be determined. With the maturation of the SLS program, computational and geometry techniques were refined, which resulted in a higher-fidelity geometry for ML-2 relative to ML-1E. Topologically, the two towers are quite similar. Both contain a base platform with a nominally rectangular truss superstructure above the platform. However, a few differences were observed, most notably with respect to the location of the elevator shaft, which is on the west side of ML-1E but on the south side of the ML-2 tower. Additionally, ML-2 is more porous than ML-1. Finally, in the production environment, ML-2 is slightly taller than ML-1. This is necessary because the Block 1B vehicle requires a larger tower than that for the smaller Block 1 rocket.

Numerical results from Kestrel were obtained and analyzed to quantify the vehicle aerodynamic effects resulting from the presence of either tower. A database was generated with the vehicle on the pad, resulting in α_P of 90 deg, for ground-wind azimuth angles (ϕ_{azi}) from 0 to 360 deg at 30 deg increments. The data yielded surface pressure coefficients, integrated surface lineloads, and integrated force and moment coefficients. The representative surface C_p data for the

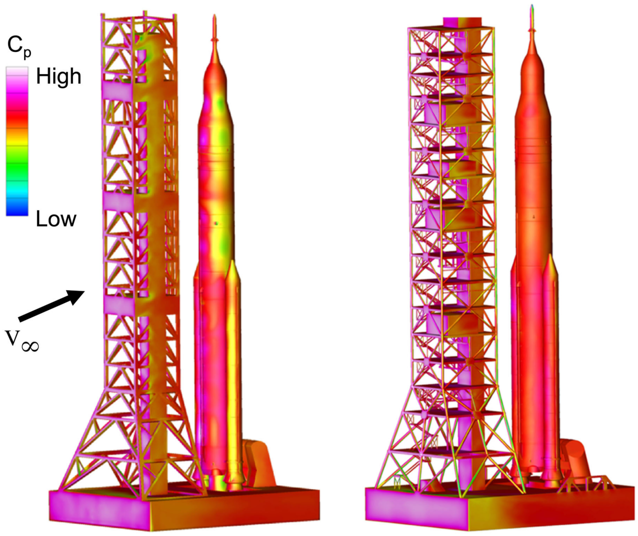

a) ML-1E b) ML-2

Fig. 22 Surface C_p with wind from the north ($\phi_{\text{azi}} = 0$ deg) in proximity to ML-1E and ML-2.

vehicle next to either tower are shown in Fig. 22 at $\phi_{\text{azi}} = 0$ deg. For this simulation, the rocket is downstream of, and thus in the wake of, the mobile launch tower. Unlike the case for ML-2, the data for ML-1E, shown in Fig. 22a, indicate a strong low-pressure region on the port side of the vehicle core and port SRB. This region has decreased pressure relative to the ML-2 solution. In this particular freestream condition, such an effect can be attributed to the flow separation from the edges of the ML-1E west-side elevator shaft, which affects the port side of the vehicle. Conversely, the presence of the south-side location of the ML-2 elevator shaft shields the vehicle against incoming northerly ground wind. This effect eliminates any large C_p gradients on the port side of the vehicle.

The lineload distributions of the normal and side force coefficients are plotted in Fig. 23. In the plot, the ML-1E data are shown as solid lines with ML-2 depicted as dashed lines. Color-coded lines correspond to the centerbody, starboard SRB, and port SRB. An axis label is provided at a value of 0. In general, a vehicle in proximity to ML-2 is subjected to decreased loads relative to the ML-1E case. This observation is especially evident when considering the forces acting on the centerbody, seen as a shift toward the 0 mark. Similar to the surface C_p data, the decreased loading on the centerbody is in large part due to the large wake behind the elevator shaft located at the south side (or furthest downstream for this condition) of the tower. The wake downstream of the south-located elevator shaft on the ML-2 tower shields the centerbody, thus decreasing the loading on this component relative to the core and ML-1E tower.

Figure 24 shows the integrated, time-averaged C_N and C_Y on the Block 1B Crew vehicle for a range of azimuthal angles. This plot presents data at all computed conditions, which comprises a range of ϕ_{azi} for given freestream conditions. Similar to the previously discussed data, the vehicle is unloaded when in proximity to ML-2 relative to ML-1E, primarily at low ϕ_{azi}. It is evident that the wake from the elevator shaft affects the flow at not only $\phi_{\text{azi}} = 0$ deg but at angles in excess of 45 deg from the zero azimuth angle case.

B. Atmospheric Boundary Layer

The overall aerodynamic characteristics of the vehicle in proximity to the ground can be quantified by using uniform flow inputs, as presented previously. In a real-world situation, the rocket and tower are subjected to a large atmospheric boundary layer. Analysis with different nonuniform freestream conditions can rapidly increase the size of these delivered databases; thus, care must be taken when developing the associated run matrix. It is possible to simulate atmospheric boundary layers in Kestrel, although this is nuanced and not simple when executed as of version 10.3. In particular, the

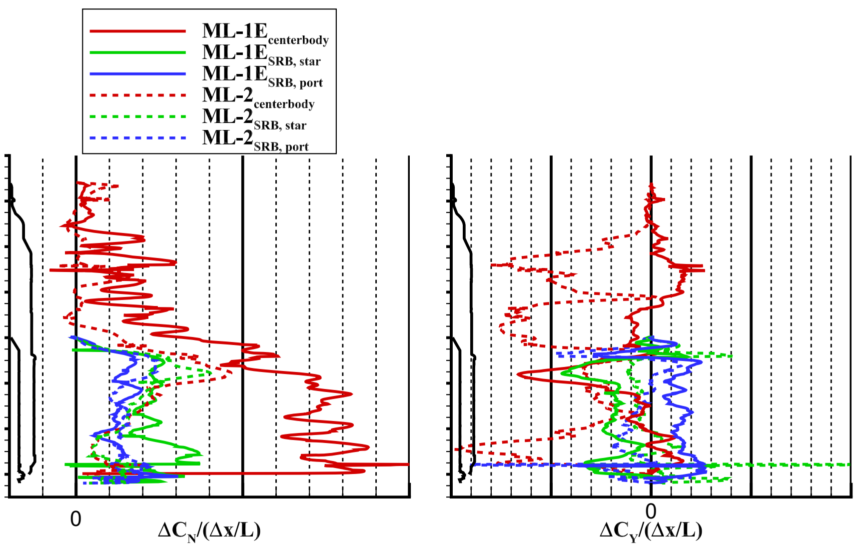

a) Normal force coefficient lineload b) Side force coefficient lineload

Fig. 23 Integrated lineloads on the Block 1B Crew vehicle mounted on two Mobile Launchers at $h/L = 0$ and $\phi_{\text{azi}} = 0$ deg, including a) $\Delta C_N/(\Delta x/L)$ and b) $\Delta C_Y/(\Delta x/L)$.

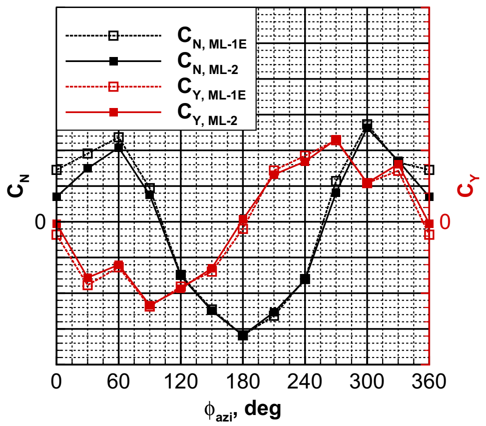

Fig. 24 Time-averaged normal and side force coefficients exerted on the Block 1B Crew vehicle mounted on two different Mobile Launchers at $h/L = 0$ and $\alpha_P = 90$ deg.

nonuniform boundary-layer profile must be imposed on the inflow boundary of an unstructured grid rather than on the Cartesian grid aligned with one of the three coordinate axes (x, y, and z). Because the boundary layer cannot be prescribed on a Cartesian grid, simulations must be executed with a fully unstructured formulation. As the unstructured grid is neither trimmed nor overlapped with a Cartesian grid, adaptive mesh refinement using such an approach is not possible. With this approach in Kestrel, the velocity flowfield with the atmospheric boundary-layer profile can be imposed at the upstream boundary for roll angles of 0, 90, 180, or 270 deg, corresponding to winds from the north, east, south, or west, respectively. For all other roll angles that are not multiples of 90 deg, the unstructured grids for the vehicle and tower must be rotated relative to the outer boundary unstructured grid and Cartesian grid to provide an adequately developed atmospheric boundary layer. Although not desirable, a three-mesh formulation could be executed that would include the inner unstructured grid, an overlapped adaptive Cartesian grid, and an unstructured farfield boundary condition. Experience has shown that this approach can yield challenging hole cutting and domain connectivity; therefore, it was not pursued.

The ground-wind profiles were selected as maximum values to ensure the integrity of the rocket and all subsystems at the specified worst-case scenario. The atmospheric boundary layer for the simulation was developed from standard previously defined SLS specifications [54]. In particular, the Design Specification for Natural Environments (DSNE) wind profiles were used. The wind-velocity profiles are specified by Eq. (5), in which u is the wind speed, $u_{18.3}$ is the velocity at 18.3 m (60.0 ft), and z is the elevation in meters:

$$u(z) = u_{18.3}\left(\frac{z}{18.3}\right)^{1.42(u_{18.3})^{-3/4}} \tag{5}$$

Based on this equation, four DSNE velocity profiles in metric units are shown in Fig. 25. These profiles correspond to the extreme conditions permissible during the four prelaunch/launch stages. These conditions include cases in which the vehicle is being transported to the launch complex, prelaunch before fueling, prelaunch after fueling, and launch. For reference, a thick, black, dotted horizontal line is shown

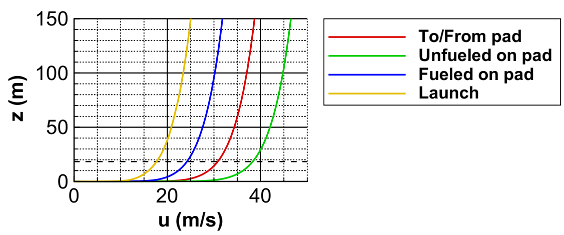

Fig. 25 Limiting DSNE atmospheric boundary-layer profiles for prelaunch and launch.

at 18.3 m (60.0 ft). As shown in the image, the most stringent constraint is at launch ($u_{18.3} = 17.7$ m/s; 39.6 mph), then a fully fueled vehicle on the pad ($u_{18.3} = 24.2$ m/s; 54.1 mph), followed by unfueled transport between the VAB and launch complex ($u_{18.3} = 30.8$ m/s; 68.9 mph), and finally the unfueled vehicle on the launch pad ($u_{18.3} = 38.3$ m/s; 85.7 mph). For all profiles, the velocity rapidly increases in magnitude from the no-slip condition on the ground to a short distance above the ground, that is, 15 m. Above this elevation, the freestream velocity gradually increases to the maximum velocity at the top of the profile used in this analysis. Note that the velocity does not asymptotically approach a constant value at high elevations. That is, a gradient in velocity as a function of altitude is finite at the maximum elevation for the SLS analysis.

Preliminary reasoning suggested that when considering aerodynamic coefficients normalized by local dynamic pressure, the effect of an atmospheric boundary-layer profile, instead of a uniform velocity profile, was less important than other parameters of interest (e.g., angle of attack, roll angle, and the vehicle and tower geometry). Consequently, it was decided to simulate one of the more stressing DSNE wind profiles to determine an estimate of the differences between cases with and without an atmospheric boundary layer. Of particular interest was the aerodynamic loading on the forward attach bracket, in which the maximum loads were exerted at ϕ_{azi} of 270 deg. In addition to this loading constraint, winds from ϕ_{azi} at 0 and 180 deg (from the north and south, respectively) would have significant vehicle/tower interactions. Therefore, it may be difficult to isolate the effect of an atmospheric boundary layer at these azimuth angles. On the other hand, winds from ϕ_{azi} of 90 and 270 deg (from the east and west, respectively) would likely result in substantial vehicle/tower interactions. Consequently, these conditions would exhibit larger differences between the atmospheric boundary layer and constant-velocity profile simulations than differences for a case in which ϕ_{azi} was either 0 or 180 deg. Because of the maximum loading on the attach hardware and decreased vehicle/tower interactions, a single simulation was executed at ϕ_{azi} of 270 deg.

The sectional lineloads exerted on the core, quantified by the side force and normal force for the two cases of interest, are plotted in Fig. 26. In these plots, the uniform velocity profile data are shown in red, and the atmospheric boundary-layer case is shown in blue. The standard nondimensional lineloads were converted to dimensional values to compare the total loading on the vehicle using both analysis methods. The uniform velocity case (blue) was scaled by the local dynamic pressure such that the dimensional forces could be determined. Conversely, the atmospheric boundary-layer simulation (red) was scaled using freestream dynamic pressure. The lineloads between the two cases are quite similar near the top of the rocket, including the upper stage, LVSA, and the top portion of the centerbody. However, differences in both the side and normal forces were observed over the upper portion of the centerbody, especially in the side force. In this region, the atmospheric boundary layer yields more side force relative to the uniform freestream case. In the same figure,

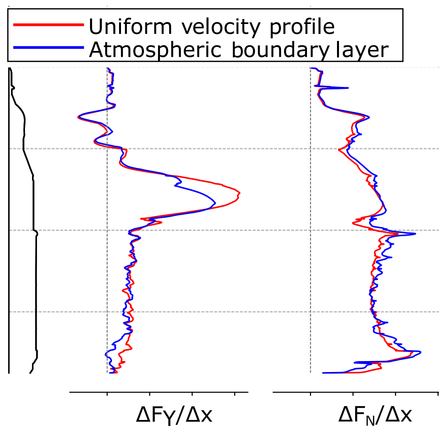

Fig. 26 Dimensional lineloads on SLS Block 1B Crew vehicle, including side and normal forces.

the normal force lineload shows similar behavior over the upper stage, LVSA, and the upper portion of the centerbody, slightly further down the rocket than the side force. However, a reduction in the normal force for the atmospheric boundary-layer case relative to the uniform freestream solution was observed near the SRB noses. Similar agreement was observed over the lower portion of the rocket.

C. Crew Access Arm

In addition to ensuring that the vehicle performance is acceptable in the low-speed regime of flight, the safety of the crew must also be satisfied at all times. In particular, a safe emergency egress from the rocket must be ensured, as discussed in Secs. II.E and II.F. The CAA is a feature that provides access to and from the vehicle and plays a key role in emergency egress. A series of computations using the vehicle, tower, and CAA were executed using the established computational approach. These data facilitated comparisons with experimental data and provided a baseline computational aerodynamic database [31,32]. Lofts of the computational and experimental geometries are shown in Fig. 27. As shown in the figure, some simplifications were made for the CFD loft relative to the experimental model.

While analysis with a static CAA informed the aerodynamic database at different CAA deployment angles and wind directions, the inherently unsteady nature of a moving CAA is most accurately represented by a moving-body simulation. With a deployment time of 45 s, a high-fidelity solution of a full configuration and tower for 45 s is extraordinarily expensive because it would require nearly a month with 3600 processors to execute only one simulation. Consequently, simplifications were made for a tractable simulation. In addition to a simplified geometry, an analysis was performed with a static CAA in the presence of the vehicle and tower for numerous deployment angles [31]. A single run was executed with a moving CAA in isolation from both the tower and vehicle.

Instead of providing a database with a range of wind azimuth and CAA deployment angles, data were provided in a new relative wind coordinate system. As shown in Eq. (6), the relative wind angle Θ is the difference between the CAA deployment angle γ and the wind azimuth angle ϕ_{azm}:

$$\Theta = \gamma - \phi_{\mathrm{azm}} \tag{6}$$

This approach significantly reduces the number of computational simulations needed for the requisite database. Figure 28a shows the normalized C_Y, side force in the CAA-fixed coordinate system. In this coordinate system, C_Y moves with the body and is the aerodynamic force that causes the CAA to swing, and the value is normalized by the maximum magnitude of C_Y for the dynamic CAA simulation. The deployment angle Θ ranges from 0 to 90, in which it is considered to be fully deployed at 0 deg with 90 and 270 deg oriented normal to the freestream flow. In the plot, the four datasets include the 1) static, isolated CAA; 2) static, full configuration, deployed CAA; 3) dynamic isolated CAA; and 4) experimental 14×22 data. Overall, good agreement was found among the four datasets with maximum loading when the CAA is perpendicular to or deployed slightly further than the incoming flow. The reasonably good agreement, especially across the dynamic CAA range of Θ, brings confidence to the analysis with both the isolated CAA and simplified-geometry full configuration analysis. An instantaneous Mach slice through the dynamic CAA simulation is shown in Fig. 28b. A large, separated wake downstream of the CAA encapsulates the importance of adaptive mesh refinement based on both the unsteady flow and unsteady body.

D. LAS Hatch Opening

The CAA serves as access from the tower to the rocket, whereas the hatch system provides access from the end of the CAA into the

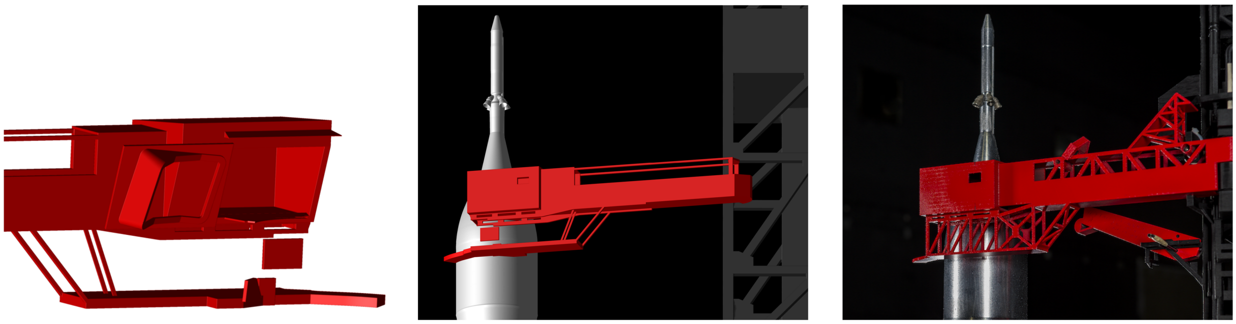

a) Isometric view of isolated CAA

b) Simulated vehicle (gray), tower (black), and CAA (red)

c) Experimental model

Fig. 27 Lofts and geometry used for CAA analysis.

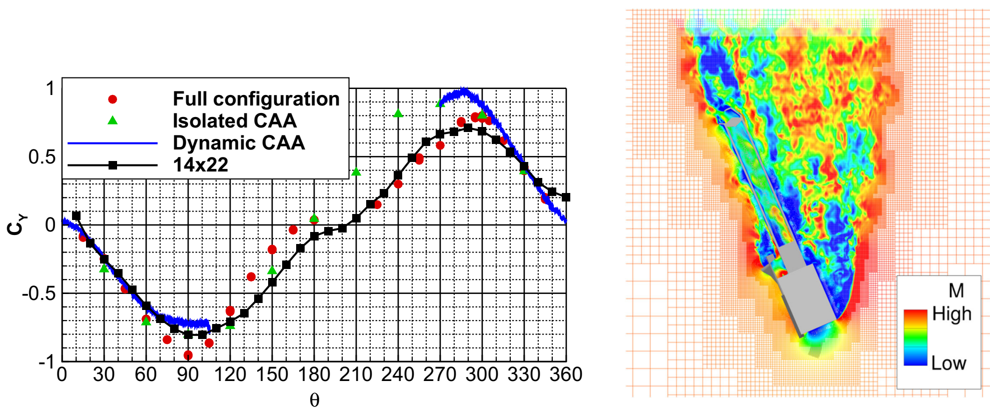

a) Experimental and computational C_Y

b) Instantaneous slice of Mach

Fig. 28 Computational and experimental results for CAA analysis.

vehicle. While exiting from the vehicle, whether in an emergency situation or not, the astronauts pass through the double-hatch system and through the CAA before entering the tower [6]. The hatch system comprises the Orion hatch and the larger LAS hatch. Both hatches deploy simultaneously. The larger, outer LAS hatch is exposed to the largest wind loads when the access door is retracted, allowing the freestream flow into the room and impinge on the LAS hatch, which is of particular concern to the program. Consequently, aerodynamic databases were provided for the forces and moments exerted upon the LAS hatch as a function of the wind direction and hatch deployment angle.

To generate high-fidelity loads, simulations were executed with four components: tower, vehicle, CAA, and hatch. The hatch is never deployed if the CAA is fully retracted; therefore, simulations were performed with the CAA in the fully deployed position, however, with the door retracted. The requested data corresponded only to the aerodynamic loads on the hatch, and integrated forces and moments were not required for either the vehicle or tower. Because loads were only needed on the hatch, the computational region of interest was a small subset of the entire computational model. As the hatch geometry is both small and very high on the launch vehicle, some geometric simplifications were made to reduce the computational cost. The full model is shown in Fig. 29a, which includes the modeled tower (black), vehicle (gray), and CAA (red). As shown in the image, the tower geometry was truncated below a body station approximately in the middle of the vehicle. In this region, the truss structure was removed, but the elevator shaft was retained. In addition to the tower simplifications, both SRBs were removed from the model.

While the lower part of the tower and boosters certainly have an impact on the resulting aerodynamic flowfield, the air near the hatch and CAA will be minimally affected by flow that is more than 100 ft away from the geometry of interest. The LAS hatch was modeled as a surface near a watertight rocket geometry, as shown in Fig. 29b. In reality, an open LAS hatch exposes the interior of the Orion vehicle to the outside environment and will have an effect on the aerodynamic loading of the hatch, but it is deemed second order. The actual region between the Orion vehicle and the LAS contains a positive pressure relative to the outside air. Consequently, this pressure generates an outward force on the LAS hatch, which will then provide an assistive hatch opening moment in the early portion of the system deployment; thus, a watertight vehicle (without positive internal pressurization) will yield a conservative result relative to the true solution. In addition, modeling an internal cavity in the simulation would greatly increase the geometric and computational complexity of the analysis. Because a closed vehicle yields a conservative aerodynamic result with decreased complexity, it was decided not to model the interior geometry. Returning to the figure, numerous different hatch deployment angles θ are shown in the figure. By definition, a θ of 0 deg is when the hatch is in the fully retracted position on the side of the

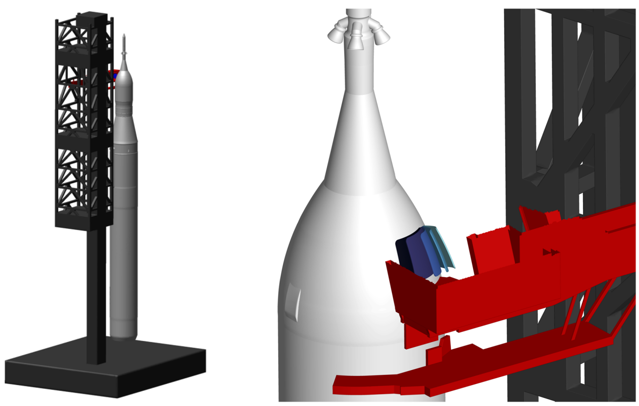

a) Wide view b) Detailed view

Fig. 29 Computational model used for hatch systems showing the truncated tower and hatch at various deployment angles with part of the CAA blanked.

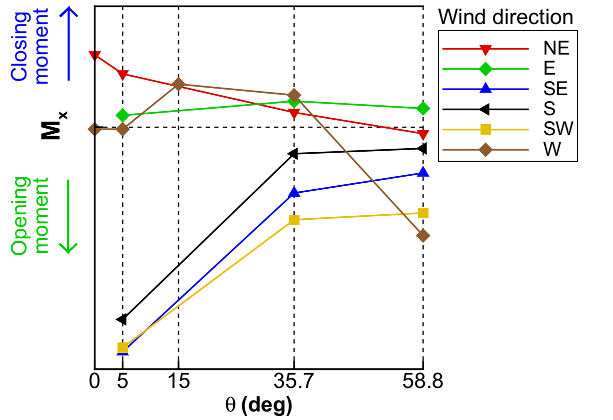

Fig. 30 Effect of hatch deployment angle and wind direction upon the hatch hinge opening moment M_x.

rocket, whereas positive values of θ exist with increasing deployment angles.

A database was generated for a range of hatch deployment angles and wind directions. Seven different θ values, ranging from fully closed (0 deg) to fully deployed (58.8 deg), were analyzed at 26 freestream wind angles and one freestream velocity. Although all six forces and moments certainly contribute to the loads on the hatch, the analyses showed that the total forces and moments are dominated by the normal force and a new "opening" or "closing" moment (defined as follows). The aerodynamic loads ultimately result in a net moment that either promotes deployment (referred to as an opening moment) or hinders deployment (referred to as a closing moment). A subset of this database is shown in Fig. 30, in which the hatch deployment angle θ is labeled on the x axis. Labels on the left side of the plot indicate the direction of the opening and closing moments relative to a zero-moment line. For the full database, the analysis was concentrated around cases with hatch deployment angles of 5, 35.7, and 58.8 deg. Some, but not all, cases resulted in an opening moment that would aid astronauts during an emergency egress situation. In general, an opening moment results from winds from the general southerly direction. These extreme conditions must be considered when evaluating the ability of the system to operate effectively. Ultimately, these data led the program to conclude that the hydraulic system was sized appropriately.

E. Wind-Induced Oscillation

Aerodynamic databases are provided at a Reynolds number of 615,000 based on the nominal core diameter of the model, which is the condition at which wind-tunnel and CFD runs are performed. However, the full-scale Reynolds number of the vehicle on the launch pad is more than an order of magnitude larger than the calculated database. Because this flow is dominated by large-scale separation, the effect of the Reynolds number should be investigated. Ultimately, the goal of this study is to increase the knowledge of the flowfield, thus reducing the uncertainty of the calculations and increasing the confidence in the provided database.

The aerodynamics of SLS on the launch pad, which include significant shedding from the surface of the rocket, may result in mode excitation that corresponds to a structural mode. The resulting fluid/structure interaction is referred to as the wind-induced oscillation (WIO). Studies of large, multibody cylinders at SLS-scale Reynolds numbers have not been executed previously; therefore, the flowfield was investigated for three reasons: 1) to provide direct support the program, 2) facilitate technology development and 3) inform a planned test in the Transonic Dynamics Tunnel.

Because this WIO analysis yielded information on the governing flowfield and SLS, it was decided to simulate an SLS-inspired geometry. This vehicle, referred to as threebody-5, has similar nondimensional ratios as SLS, all normalized to a core diameter of 100 in. To investigate the underlying physics and understand the scaling effects on the flowfield, a Reynolds number sweep, independent of

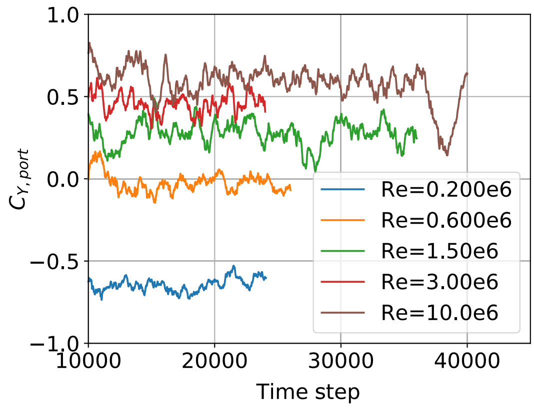

Fig. 31 Time histories of $C_{n,\text{port}}$ for Reynolds number sweep of three-body-5 vehicle.

the Mach number, was performed. As separation is a strong function of the Reynolds number, it was surmised that the Reynolds number may also affect the Coanda state. The time history of the side force on the port SRB at Mach 0.183 for five different Reynolds numbers is shown in Fig. 31. Although Mach 0.183 is larger than typical wind speeds, this Mach number was selected to be in alignment with wind-tunnel tests that were executed under these conditions. As shown in the figure, overall, an increased Reynolds number corresponds to an increase in $C_{Y,\text{port}}$. Notably, $C_{Y,\text{port}}$ is negative for a Reynolds number of 200,000, nearly 0 for 600,000, and positive for all other Reynolds numbers. This observation indicates a Coanda mode flip for 200,000 relative to the other three cases. As the Coanda mode changes with the Reynolds number, it may be significant to supply aerodynamic databases at both the wind-tunnel and flight Reynolds numbers. Such a discussion can be pursued with the upcoming development of Block 2 configuration.

VII. Conclusions

This review paper includes a summary of the computational efforts from the NASA Langley Research Center to predict the low-speed flight characteristics of the SLS vehicle. The particular region of interest ranges from when the vehicle is on the launch pad to Mach 0.3, when ascent is defined to begin. In this relatively short period of flight, the vehicle is exposed to a wide range of conditions, including angles of attack ranging from 0 to 90 deg and 360 deg of roll angle. The high-alpha conditions on a three-body vehicle result in an extraordinarily complex flowfield that includes a variety of flowfield features, such as asymmetric vortices and the Coanda effect. To resolve these flowfields accurately, complex IDDES computations coupled with an adaptive grid were executed using the Kestrel CFD program developed by the DOD HPCMP CREATE-AV group.

Computational methods have been developed such that academic-fidelity computations are executed in a production environment. This rare approach is necessary to provide high-quality aerodynamic databases to other SLS subteams. Databases were calculated for both the isolated vehicle and vehicle in close proximity to the launch tower. Through exhaustive efforts, it was ultimately concluded that the adaptive mesh routines must be employed at least 1.5 core diameters downstream of the leeward edge of the vehicle. This level of offbody refinement is necessary to ensure that a proper surface pressure distribution is predicted for the rocket. As with any large-scale computational effort, the fidelity of the simulation, and thus the extent of grid refinement, must be balanced with the available computational resources. It was also confirmed that the time step for these simulations must be sufficiently small such that the nondimensional time step is less than 0.01, which is a general guideline accepted in the CFD community.

The uncertainty quantification of computational datasets is still limited to external comparisons, usually code-to-code and code-to-tunnel frameworks. Quantification of uncertainty on distributed load datasets, such as lineloads, remains an active area of research, as does the improvement of uncertainty quantification on integrated quantities of interest, which are primarily sourced from computational data. Data fusion and sensitivity studies remain promising avenues through which computational datasets can be more rigorously bounded for future SLS generations. With a large-scale program extending over many years, improvements to computational solvers, at times significant, have resulted in various versions of the code being executed for different databases. The numerical results from different code versions, although close, are not identical. Although the consistency of the analysis is paramount, these differences contribute a not insignificant amount of uncertainty to the system.

In the future, it will be desirable to have an improved understanding of the aerodynamics of multibody vehicles. Although some experimental studies have investigated the Coanda effect on the SLS, an extensive computational study has not been conducted. Consequently, unsteady simulations will be performed on both a two-dimensional three-body cylinder geometry and an SLS vehicle. Of particular interest is the flow between the gaps and in the wake for Reynolds numbers as low as 200,000 and as high as 10 million. An ongoing effort is focused on the effect of roughness on a simplified SLS model. Instead of a computational roughness model, surface mesh-scale artificial roughness is being applied to understand the turbulent wake development. Finally, the fluid–structure interactions of an SLS vehicle geometry will be computed using Kestrel and compared to experimental data. A structural response model is available in Kestrel for a user-provided geometry.

Computational support will continue to be critically important for the success of the SLS program. Following the launch of Artemis I, careful comparisons will be made between the flight data and computational results. The lessons learned will carry forward into the SLS program. The development of SLS vehicles will continue in the future. Similar low-speed computational support will be provided for the Block 1B and Block 2 vehicles. This will include database development for the full vehicle and any other trade study support and program requirements. In addition, the development of unsteady lineloads is planned to inform the Ground Wind Loads database. As the SLS program matures, the computational tools for the low-speed regime have been systematically refined. Nearly 10 years of efforts, extending back to the time period immediately after the end of the Constellation program, have resulted in exhaustive support for the SLS program. Best-practice standards will continue to be refined in the future to ensure the delivery of high-quality databases to the program.

Acknowledgments

The information presented in this survey paper is a small representation of the efforts to predict the aerodynamics of launch vehicles in the early phases of flight. Although the computational team members have changed over the years, the core vision of the group remained unwavering. In addition to the authors, other team members include Nalin Ratnayake, Craig Streett, Oleg Goushcha, Jeremy Pinier, Patrick Shea, Jesse Collins, Amber Favaregh, Ethan Vogel, Brianna Blocher, Varda Ahmed, Satvik Kumar, and Chris Eggert.

References

[1] Anon., *Artemis Plan: NASA's Lunar Exploration Program Overview*, NASA, Sept. 2020, https://www.amazon.com/Artemis-Plan-Exploration-Program-Overview/dp/B0B5Y5ZQ16.

[2] Blevins, J. A., Campbell, J. R., Jr., Bennett, D. W., Rausch, R. D., Gomez, R. J., and Kiris, C. C., "An Overview of the Characterization of the Space Launch System Aerodynamic Environments," *AIAA Aerospace Sciences Meeting*, AIAA Paper 2014-1253, Jan. 2014. https://doi.org/10.2514/6.2014-1253

[3] Pinier, J. T., Herron, A. J., and Gomez, R. J., "Advances in the Characterization of NASA's Space Launch System Aerodynamic Environments," *AIAA AVIATION Forum*, AIAA Paper 2019-3397, June 2019. https://doi.org/10.2514/6.2019-3397

[4] Donahue, B., "The Space Launch System: Development Progress," *AIAA SPACE Forum*, AIAA Paper 2016-5415, Sept. 2016. https://doi.org/10.2514/6.2016-5415

[5] Pomeroy, B. W., Krist, S. E., and Wignall, T. J., "Sensitivity of Space Launch System Low-Speed Aerodynamic CFD Results to Kestrel Flow Solver Inputs," NASA TP-20230003697, 2023.
[6] Pomeroy, B. W., Krist, S. E., Wignall, T., Deere, K. A., Lee, M. W., Ghaffari, F., Collins, J. G., Ratnayake, N. A., Streett, C. L., Goushcha, O. O., et al., "An Overview of NASA Langley Low-Speed CFD Contributions to the Space Launch System Program," *AIAA SciTech Forum*, AIAA Paper 2016-0236, 2016.
https://doi.org/10.2514/6.2023-0236
[7] Anon., SLS-SPEC-048: Cross-Program Integrated Coordinate Systems, Revision F.1, 2018.
[8] Chan, D. T., Paulson, J. W., Jr., Shea, P. R., Toro, K. G., Parker, P. A., and Commo, S. A., "Aerodynamic Characterization and Improved Testing Methods for the Space Launch System Liftoff and Transition Environment," *AIAA AVIATION Forum*, AIAA Paper 2019-3398, June 2019.
https://doi.org/10.2514/6.2019-3398
[9] Chan, D. T., Shea, P. R., Goodliff, S., Walker, M. A., Collins, J. G., Langston, S. L., Mears, L. J., Rieken, E., and Pinier, J. T., "Overview of the High Reynolds Number Ascent Wind Tunnel Test of the Space Launch System at the National Transonic Facility," *AIAA SciTech Forum*, AIAA Paper 2023-0425, Jan. 2023.
https://doi.org/10.2514/6.2023-0425
[10] Shea, P. R., Chan, D. T., Walker, M. A., Langston, S. L., Collins, J. G., Mears, L. J., Rieken, E., and Pinier, J. T., "Force and Moment Analysis for the High Reynolds Number Wind Tunnel Test of the Space Launch System at Ascent Conditions," *AIAA SciTech Forum*, AIAA Paper 2023-0426, Jan. 2023.
https://doi.org/10.2514/6.2023-0426
[11] Ramey, J. M., Giles, I. M., Goushcha, O. O., Heaney, P. S., Piatak, D. J., Sekula, M. K., and Soranna, F., "Parametric Study of the Forward Attachment Geometry for the Space Launch System Next Generation Booster," *AIAA SciTech Forum*, AIAA Paper 2023-0427, Jan. 2023.
https://doi.org/10.2514/6.2023-0427
[12] Dalle, D. J., "Launch Vehicle Aerodynamics Database Development for SLS," *NASA Advanced Supercomputing (NAS) Division Advanced Modeling and Simulation (AMS) Series*, ARC E-DAA-TN52395, March 2022.
[13] Dalle, D. J., Rogers, S. E., Meeroff, J. G., Burkhead, A. C., Schauerhamer, D. G., and Diaz, J. F., "Launch Vehicle Ascent CFD for the Space Launch System," *AIAA SciTech Forum*, AIAA Paper 2023-0237, Jan. 2023.
https://doi.org/10.2514/6.2023-0237
[14] Meeroff, J. G., Dalle, D. J., Rogers, S. E., Burkhead, A. C., Schauerhamer, D. G., and Diaz, J. F., "Advances in Space Launch System Booster Separation CFD," *AIAA SciTech Forum*, AIAA Paper 2023-0238, Jan. 2023.
https://doi.org/10.2514/6.2023-0238
[15] Pomeroy, B. W., and Krist, S. E., "Validation of Kestrel IDDES Simulations for SLS Transition Analysis," *AIAA SciTech Forum*, AIAA Paper 2022-1335, Jan. 2022.
https://doi.org/10.2514/6.2022-1335
[16] Pomeroy, B. W., "NASA Langley Low-Speed CFD Contributions to the Space Launch System Program," *NASA Advanced Supercomputing (NAS) Division Advanced Modeling and Simulation (AMS) Series*, NASA Ames Research Center, Moffett Field, CA, May 2022, https://www.nas.nasa.gov/pubs/ams/2022/05-19-22.html.
[17] Pomeroy, B. W., "A Seminar: NASA Langley Low-Speed CFD Contributions to the Space Launch System Program," Clarkson Univ. Graduate Seminar Series, Nov. 2022.
[18] Walker, M. A., Pinier, J. T., Shea, P. R., Collins, J. G., Mears, L. J., Lee, M. W., and Pomeroy, B. W., "Experimental Identification of Bistable Flow States on the Space Launch System at Liftoff Conditions," *AIAA AVIATION Forum*, AIAA Paper 2022-3665, July 2022.
https://doi.org/10.2514/6.2022-3665
[19] Ratnayake, N. A., Krist, S. E., Ghaffari, F., and Deere, K. A., "Computational Fluid Dynamics Methods Used in the Development of the Space Launch System Liftoff and Transition Lineloads Databases," *AIAA AVIATION Forum*, AIAA Paper 2019-3399, June 2019.
https://doi.org/10.2514/6.2019-3399
[20] Wignall, T., "Liftoff and Transition Database Generation for Launch Vehicles Using Data-Fusion-Based Modeling," *AIAA AVIATION Forum*, AIAA Paper 2019-3401, June 2019.
https://doi.org/10.2514/6.2019-3401
[21] Krist, S. E., Ratnayake, N. A., and Ghaffari, F., "Kestrel Results at Liftoff Conditions for a Space Launch System Configuration in Proximity to the Launch Tower," *AIAA AVIATION Forum*, AIAA Paper 2019-3400, June 2019.
https://doi.org/10.2514/6.2019-3400
[22] Eggert, C. A., Shea, P. R., Ratnayake, N. A., and Krist, S. E., "Effect of Sting Geometry on Axial Force Calculation for the Space Launch System," *AIAA AVIATION Forum*, AIAA Paper 2019-2126, June 2019.
https://doi.org/10.2514/6.2019-2126
[23] Fidler, J., and Bateman, M., "Asymmetric Vortex Effects on Missile Configurations," *Journal of Spacecraft and Rockets*, Vol. 12, No. 11, 1975, pp. 674–681.
https://doi.org/10.2514/3.57034
[24] Hunt, B., "Asymmetric Vortex Forces and Wakes on Slender Bodies," *AIAA Atmospheric Flight Mechanics Conference*, AIAA Paper 1982-1336, Aug. 1982.
https://doi.org/10.2514/6.1982-1336
[25] Degani, D., and Schiff, L. B., "Computation of Turbulent Supersonic Flows Around Pointed Bodies Having Crossflow Separation," *Journal of Computational Physics*, Vol. 66, No. 1, 1986, pp. 173–196.
https://doi.org/10.1016/0021-9991(86)90059-8
[26] Bridges, D. H., "The Asymmetric Vortex Wake Problem—Asking the Right Question," *AIAA Fluid Dynamics Conference and Exhibit*, AIAA Paper 2006-3553, June 2006.
https://doi.org/10.2514/6.2006-3553
[27] Wignall, T., Walker, M. A., and Collins, J. G., "Experimental and Computational Examination of the Coanda Effect on the Space Launch System at Liftoff Conditions," *AIAA SciTech Forum*, AIAA Paper 2023-0236, Jan. 2023.
[28] Parks, E., and Peterson, R., "Analysis of a 'Coanda' Type Flow," *AIAA Journal*, Vol. 6, No. 1, 1968, pp. 4–7.
https://doi.org/10.2514/3.4433
[29] Levinsky, E. S., and Yeh, T. T., "Analytical and Experimental Investigation of Circulation Control by Means of a Turbulent Coanda Jet," NASA CR-2114, 1972.
[30] Mears, L. J., Shea, P. R., Collins, J. G., Langston, S. L., Walker, M. A., and Pinier, J. T., "Experimental Characterization of the Space Launch System Block 1B Liftoff and Transition Environment," *AIAA SciTech Forum*, AIAA Paper 2023-0423, 2023.
https://doi.org/10.2514/6.2023-0423
[31] Wignall, T., Collins, J. G., and Pomeroy, B. W., "Ground Wind Loads on the Space Launch System Mobile Launcher Crew Access Arm," *AIAA SciTech Forum*, AIAA Paper 2023-0240, Jan. 2023.
https://doi.org/10.2514/6.2023-0240
[32] Collins, J. G., Mears, L. J., Shea, P. R., Langston, S. L., Walker, M. A., and Pinier, J. T., "Improved Techniques for Measuring Static Ground Wind Loads on the NASA Space Launch System Mobile Launcher 2," *AIAA SciTech Forum*, AIAA Paper 2023-0424, Jan. 2023.
https://doi.org/10.2514/6.2023-0424
[33] Angel, J. B., Neuhoff, S., Wong, M. L., Barard, M. F., and Kiris, C. C., "Predicting SLS Launch Environment Using a Novel Multiphase Formulation," *AIAA SciTech Forum*, AIAA Paper 2023-0645, Jan. 2023.
https://doi.org/10.2514/6.2023-0645
[34] Krist, S. E., and Ghaffari, F., "Detached Eddy Simulation Results for a Space Launch System Configuration at Liftoff Conditions and Comparison with Experiment," *AIAA SciTech Forum*, AIAA Paper 2015-0776, Jan. 2015.
https://doi.org/10.2514/6.2015-0776.10.2514/6.2015-0776
[35] Ratnayake, N. A., Krist, S. E., Ghaffari, F., and Ahmed, V., "Unstructured Grid Development for the Space Launch System Liftoff and Transition Lineloads Computational Analysis," *AIAA SciTech Forum*, AIAA Paper 2020-0672, Jan. 2020.
https://doi.org/10.2514/6.2020-0672
[36] McMillin, S. N., Shea, P. R., Dalle, D. J., Rogers, S. E., Roozeboom, N. H., Meeroff, J. G., and Lee, H. C., "Comparison of Space Launch System Aerodynamic Surface Pressure Measurements from Experimental Testing and CFD," *AIAA AVIATION Forum*, AIAA Paper 2019-2128, June 2019.
https://doi.org/10.2514/6.2019-2128
[37] Pritchett, V., Mayle, M. N., Blevins, J. A., Crosby, W. A., and Purinton, D. C., "Aerodynamic Tests of the Space Launch System for Database Development," *AIAA Aerospace Sciences Meeting*, AIAA Paper 2014-1256, Jan. 2014.
https://doi.org/10.2514/6.2014-1256
[38] Favaregh, A. L., Houlden, H. P., and Pinier, J. T., "Space Launch System Aerodynamic Database Uncertainty Quantification Methodologies," *AIAA SciTech Forum*, AIAA Paper 2016-0795, Jan. 2016.
https://doi.org/10.2514/6.2016-0795
[39] Abdol-Hamid, K., Ghaffari, F., and Parlette, E., "Ares I Vehicle Computed Turbulent Ascent Aerodynamic Data Development and Analysis," *Journal of Spacecraft and Rockets*, Vol. 49, No. 4, 2012, pp. 596–608.
https://doi.org/10.2514/1.A32112
[40] Abdol-Hamid, K., and Ghaffari, F., "Error Estimates of the Ares I Computed Turbulent Ascent Longitudinal Aerodynamic Analysis,"

Journal of Spacecraft and Rockets, Vol. 49, No. 4, 2012, pp. 609–616.
https://doi.org/10.2514/1.A32143

[41] Morton, S. A., McDaniel, D. R., Sears, D. R., Tillman, B., and Tuckey, T. R., "Kestrel—A Fixed Wing Virtual Aircraft Product of the CREATE Program," *AIAA Aerospace Sciences Meeting*, AIAA Paper 2009-0338, Jan. 2009.
https://doi.org/10.2514/6.2009-338

[42] Morton, S. A., and Meakin, R. L., "HPCMP CREATE-AV Kestrel Architecture, Capabilities, and Long Term Plan for Fixed-Wing Aircraft Simulations," *AIAA SciTech Forum*, AIAA Paper 2016-0565, Jan. 2016.
https://doi.org/10.2514/6.2016-0565

[43] McDaniel, D. R., Tuckey, T. R., and Morton, S. A., "The HPCMP CREATE-AV Kestrel Computational Environment and Its Relation to NASA's CFD Vision 2030," *AIAA SciTech Forum*, AIAA Paper 2017-0813, Jan. 2017.
https://doi.org/10.2514/6.2017-0813

[44] Anon., *HPCMP CREATE-AV Kestrel User's Guide*, HPCMP CREATE (Computational Research and Engineering Acquisition Tools and Environments), Air Vehicles, Ver. 10.3r.

[45] Samareh-Abolhassani, J., "GridTool: A Surface Modeling and Grid Generation Tool," *Proceedings of the Workshop on Surface Modeling, Grid Generation, and Related Issues in CFD Solutions*, NASA CP-3291, 1995.

[46] Frink, N., Pirzadeh, S. Z., Parikh, P. C., Pandya, M. J., and Bhat, M. K., "The NASA Tetrahedral Unstructured Software System (TetrUSS)," *Aeronautical Journal*, Vol. 104, No. 1040, 2000, pp. 491–499.

[47] Pirzadeh, S., "Structured Background Grids for Generation of Unstructured Grids by Advancing Front Method," *AIAA Applied Aerodynamics Conference*, AIAA Paper 1991-3223, 1991.
https://doi.org/10.2514/6.1991-3233

[48] Dalle, D. J., Rogers, S. E., Lee, H. C., and Meeroff, J. G., "Adjustments and Uncertainty Quantification for SLS Aerodynamic Sectional Loads," *AIAA AVIATION Forum*, AIAA Paper 2018-3640, June 2018.
https://doi.org/10.2514/6.2018-3640

[49] Dalle, D. J., Rogers, S. E., Burkhead, A. C., and Meeroff, J. G., "Distribution of SLS Integrated Load Uncertainty to Surface Pressures and Sectional Loads," *11th International Conference on Computational Fluid Dynamics (ICCFD11)*, ICCFD11-3303, 2022.

[50] Wignall, T. J., and Houlden, H., "Uncertainty Quantification for Launch Vehicle Aerodynamic Lineloads," *AIAA SciTech Forum*, AIAA Paper 2020-1521, Jan. 2020.
https://doi.org/10.2514/6.2020-1521

[51] Deere, K. A., Krist, S. E., Ratnayake, N. A., Ghaffari, F., Pomeroy, B. W., and Wignall, T. J., "Computational Techniques to Generate Space Launch System Aerodynamic Databases," *Journal of Spacecraft and Rockets*, 2023 (accepted for publication).

[52] Lee, M. W., and Wignall, T., "PCLAM: A Python Module for Computing Surface Lineloads and Moments," NASA TM-20220005189, 2022.

[53] Carlson, H., Verberg, R., Pinier, J., and Krist, S., "Reduced-Order Model for NASA Space Launch System Liftoff Aerodynamics," *AIAA Aerospace Sciences Meeting*, AIAA Paper 2015-0777, Jan. 2015.
https://doi.org/10.2514/6.2015-0777

[54] Anon., SLS-SPEC-159: Cross-Program Design Specification for Natural Environments (DSNE), Revision I, 2021.

J. Pinier
Associate Editor